Yrast and nonyrast states in ^{126}Te

Atreyee Dey,[*] A. K. Singh, and Anwesha Basu[†]
Department of Physics, Indian Institute of Technology Kharagpur, Kharagpur 721302, India

Somnath Nag
Department of Physics, Indian Institute of Technology (BHU), Varanasi 221005, India

G. Mukherjee, S. Bhattacharyya, S. Nandi,[‡] and S. Bhattacharya
Variable Energy Cyclotron Centre, Kolkata 700064, India
and Homi Bhabha National Institute, Training School Complex, Anushaktinagar, Mumbai 400094, India

R. Banik
Institute of Engineering and Management, Saltlake Sector V, Kolkata 700091, India

R. Raut, S. S Ghugre, S. Das, S. Samanta,[§] and S. Chatterjee
UGC-DAE CSR, Kolkata Centre, Kolkata 700098, India

A. Goswami[‖] and S. Ali[¶]
Saha Institute of Nuclear Physics, Kolkata 700064, India

H. Pai
Extreme Light Infrastructure - Nuclear Physics, Horia Hulubei National Institute for R&D in Physics and Nuclear Engineering, Bucharest-Magurele, 077125, Romania

S. Rajbanshi
Department of Physics, Presidency University, Kolkata 700073, India

(Received 26 May 2023; revised 4 March 2024; accepted 20 March 2024; published 30 April 2024)

The yrast and nonyrast states of ^{126}Te were populated in a fusion-evaporation reaction using a target of ^{124}Sn and α beam at 31 MeV energy. All the γ-γ coincidences were recorded using the Indian National Gamma Array at the Variable Energy Cyclotron Centre, India, and processed by a digital data-acquisition system. The level scheme was enriched with the addition of 65 new transitions and the identification of five new structures. Spin and parity assignments were made and the subsequent results were interpreted in the framework of the nuclear shell model using the large-scale shell-model code ANTOINE.

DOI: 10.1103/PhysRevC.109.044327

I. INTRODUCTION

Shape transitions and shape coexistence are widely observed in nuclei with Z or N values near closed shells. Examples include Pd ($Z = 46$) [1,2], Cd ($Z = 48$) [3,4], Xe($Z = 54$) [2], Ba ($Z = 56$) [2,5], Hg ($Z = 80$) [6,7], and Po ($Z = 84$) [8] isotopes. Nuclei near closed shells are spherical in shape, whereas they attain a deformed shape due to residual interactions between the valence nucleons, with the addition of more nucleons to it [9–11]. The interplay between these forces is responsible for the observation of shape transitions with changes in spin for these nuclei.

The Te isotopes have two protons outside the $Z = 50$ shell closure which mainly occupy the $\pi g_{7/2}$ and $\pi d_{5/2}$ orbitals while the neutrons occupy the $\nu g_{7/2}$, $\nu d_{5/2}$, $\nu d_{3/2}$, $\nu s_{1/2}$, and $\nu h_{11/2}$ orbitals. A few nucleon pairs may break and get excited to higher orbitals that generate higher spin states. In the neutron-rich Te isotopes, we observe excitations due to the breaking of neutron and proton pairs. In particular, occupation of the high-j $h_{11/2}$ intruder orbital, which has a large quadrupole moment, is responsible for the observation

[*]atreyee_dey@iitkgp.ac.in
[†]Present address: Saha Institute of Nuclear Physics, Kolkata 700064, India.
[‡]Present address: Physics Division, Argonne National Laboratory, Lemont, Illinois 60439, USA.
[§]Present address: University of Genoa, Genoa, Italy.
[‖]Deceased.
[¶]Present address: Government General Degree College at Pedong, Kalimpong, 734311 India.

of deformations in these nuclei. The proton Fermi surface lies near the low-Ω orbitals of $h_{11/2}$, resulting in a prolate shape while the neutron Fermi surface is in the medium-high Ω orbitals which results in an oblate shape. A competition between the two mechanisms results in the observation of shape changes and shape coexistence in these nuclei. Additionally, an alignment of the particles in these orbitals can result in the observation of band crossings near the yrast line [12].

The $E(4_1^+)/E(2_1^+)$ ratios for the even-mass tellurium isotopes in the mass region $A = 118$–128 lie between 1.99 and 2.09, which is close to the value of a pure vibrator (2.0), indicating a vibrational-like structure in the low-spin region of these nuclei [13,14]. However, the quadrupole moment of the $E(2_1^+)$ states is quite high and similar in magnitude to those of rotational nuclei [14,15]. Hence, a transitional behavior from a vibrational to rotational nature can be expected in these nuclei. In the framework of the interacting boson model (IBM), the Te isotopes are expected to show properties transitioning from U(5) dynamical symmetry (spherical vibrator) to O(6) symmetry (γ soft) [14,16].

The transition between U(5) and O(6) symmetries can be considered to be a second-order phase transition with the critical point being described by the E(5) symmetry [17,18]. The first experimental evidence for E(5) symmetry was in the ^{134}Ba nucleus [19]. The presence of this symmetry is determined by a few notable experimental features including the ratio $E(4_1^+)/E(2_1^+)$ being close to 2.20 [17] and $B(E2; 4_1^+ \rightarrow 2_1^+)/B(E2; 2_1^+ \rightarrow 0_1^+) \approx 1.5$ [17,20]. Both ^{124}Te and ^{126}Te have been suggested to have a possible E(5) symmetry [14].

Our motivation for the present work was to populate the yrast and near-yrast levels of ^{126}Te using the α induced heavy-ion fusion evaporation reaction. Several new γ transitions have been placed, decaying to the existing levels. In the following sections, we discuss the experimental details, data analysis techniques, main results, and discussions involving shell model calculations.

II. EXPERIMENTAL DETAILS

An experiment was conducted to populate the excited nuclear states of ^{125,126}Te using the fusion-evaporation reaction ^{124}Sn(α, $3n/2n$) ^{125,126}Te at the Variable Energy Cyclotron Centre (VECC), Kolkata, India. The ^{124}Sn target was of thickness 8.1 mg/cm^2. The α beam delivered by the K-130 cyclotron was operated at two energies, 31 and 35 MeV, to populate ^{126}Te and ^{125}Te, respectively. The γ-γ coincidences were recorded by the Indian National Gamma Array (INGA) Spectrometer, which consists of seven Compton-suppressed HPGe clover detectors. The detectors were arranged in a ring with four detectors at 90°, 2 detectors at 125°, and one at 40°. The event trigger was set to a multiplicity of 2, i.e., events would be recorded by the DAQ if two or more detectors fired at the same time. A total of 5.3×10^6 events of two- and higher-fold were recorded. A digital data-acquisition system was used, based on the PIXIE-16 (XIA LLC, USA) 12-bit 250 MHz digitizer modules running on a firmware conceptualized at UGC-DAE CSR, Kolkata Centre [21].

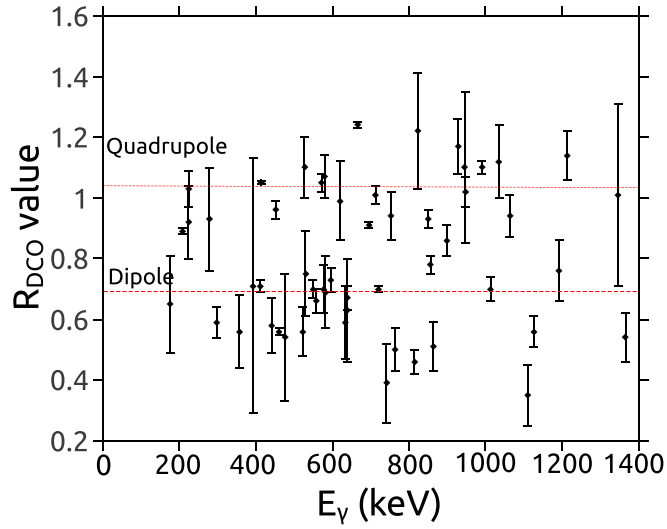

FIG. 1. The R_{DCO} values of the transitions as a function of γ-ray energy are plotted. The R_{DCO} values have been obtained in quadrupole gates. DCO value for a known stretched $E2$ transition gives a value of 1.05(1) while a pure dipole transition gives a value of 0.70(1).

III. DATA ANALYSIS

The various programs in the IUCPIX package [21] were used to process and sort the raw data into $\gamma - \gamma$ (symmetric and asymmetric) matrices and $\gamma - \gamma - \gamma$ cube.

The spins of the nuclear states were determined by calculating directional correlations of γ rays deexciting oriented states (DCO) ratios for the γ transitions [22]. The DCO ratio for γ_2 can be obtained experimentally as

$$R_{\mathrm{DCO}} = \frac{I_{\gamma_2}(\theta_1), Gate : \gamma_1 at \theta_2}{I_{\gamma_2}(\theta_2), Gate : \gamma_1 at \theta_1}$$

The experimental R_{DCO} values in the current work are 0.70(1) for a pure dipole transition and 1.05(1) for a quadrupole transition in a quadrupole gate. R_{DCO} values for known pure dipole and quadrupole transitions in the present work were used as references to assign multipolarities to the new transitions and subsequently assign spin values to the nuclear levels (Fig. 1). For the R_{DCO} measurements, two asymmetric matrices were constructed. One matrix contained events from 90° (θ_2) detectors on the x-axis and those from 125° (θ_1) detectors on the y axis and vice versa for the other matrix.

To assign definite parity to the states, we need to determine the electric or magnetic nature of the decaying transitions. This was achieved by measuring the ΔIPDCO (integrated polarization direction correlation) ratios. The ΔIPDCO ratio is defined as

$$\Delta IPDCO = \frac{\mathrm{a}(E_\gamma) N_\perp - N_\parallel}{\mathrm{a}(E_\gamma) N_\perp + N_\parallel}. \quad (1)$$

Here "$\mathrm{a}(E_\gamma)$" is the geometrical asymmetry correction factor. Here $\mathrm{a}(E_\gamma)$ has a linear dependence on E_γ, $\mathrm{a}(E_\gamma) = \mathrm{a} + \mathrm{bE}_\gamma$. For the current setup, the value of "a" was found to be 1.000(3) over a wide range of γ-ray energies, while

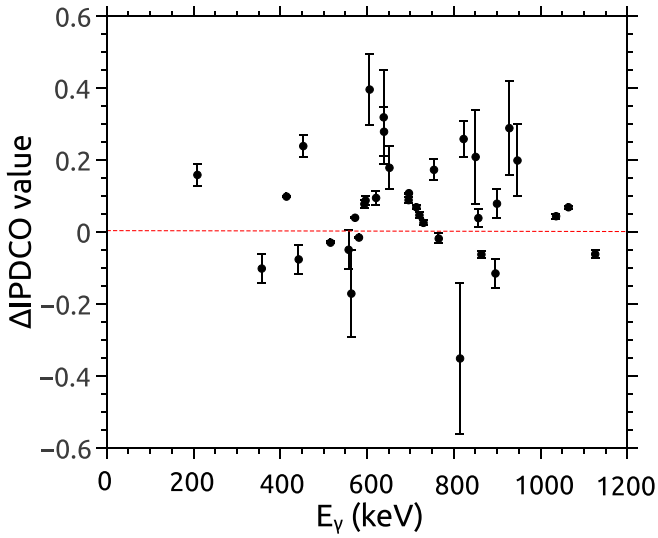

FIG. 2. The ΔIPDCO values of the transitions as a function of energy are plotted. Positive values indicate a predominantly electric-type nature whereas a negative value indicates a magnetic-type nature.

b $\approx 10^{-6}$ [23,24]. $N_\perp$ and $N_\parallel$ represent the number of γ photons scattered perpendicular and parallel to the emission plane, respectively. Two asymmetric matrices were constructed with events in the 90° detectors scattered in parallel (perpendicular) direction to the emission plane and events from all the detectors on the other axis. A positive value of ΔIPDCO indicates an electric-type transition while a negative value indicates a magnetic nature of the transition (Fig. 2).

The building of the nuclear level scheme, determination of $R_{\rm DCO}$ and ΔIPDCO values, and intensity measurements were carried out using the RADWARE package [25].

IV. RESULTS

In the present work, the previously obtained level scheme [26–28] has been confirmed and further expanded with the placement of 65 new transitions (Table I). The complete level scheme obtained in the present work is shown in Figs. 3 and 4. The level scheme has been split into two for clarity. Some of these transitions have been identified as extensions of the previously existing band structures and feeding into the ground and negative-parity bands. The intensities of the transitions were normalized with respect to the 666.3-keV γ transition for which the intensity was taken to be 1000. A few of the γ-ray intensities could not be determined due to several transitions having overlapping energy values or the absence of a normalizing transition in a gate.

The $R_{\rm DCO}$ and IPDCO values were used to assign multipolarities of the transitions and, subsequently, the spin and parity of the energy levels. Transitions with negative values of the ΔIPDCO were assigned a magnetic nature and those with a positive value were assigned an electric nature. Since $M1$ transitions are usually accompanied by a small admixture of $E2$, these transitions have been designated as $M1(+E2)$. For

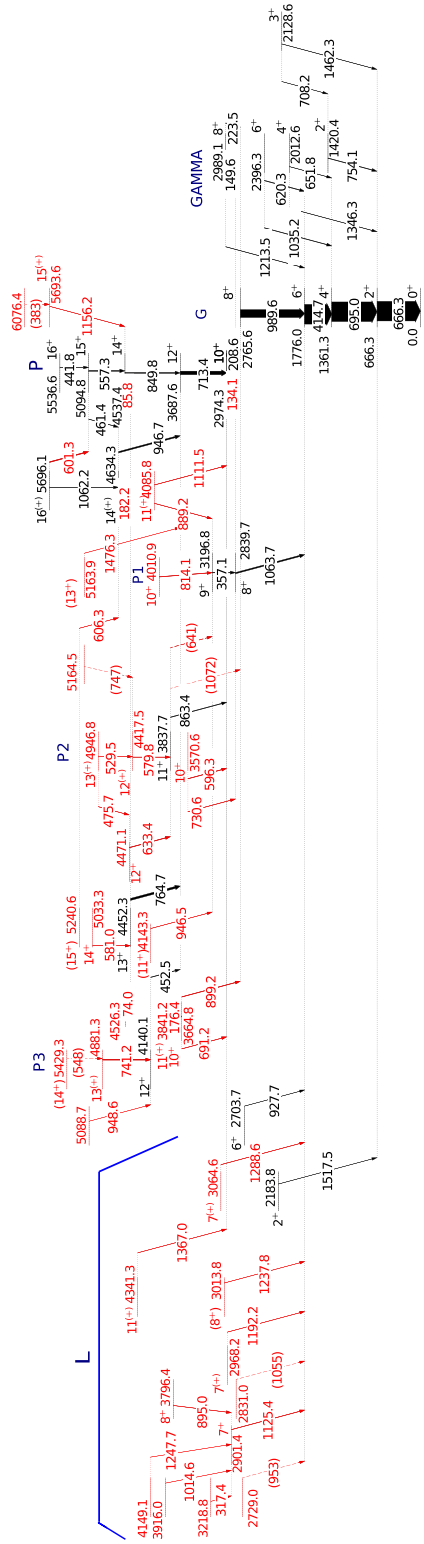

FIG. 3. The positive-parity section of the level scheme of ^{126}Te as obtained in the present work. The new γ rays and levels are marked in red.

γ rays where ΔIPDCO measurements were not possible, the assigned multipolarity is $M1 + E2$. In the following section, we discuss in detail some of the observations from this work.

TABLE I. Initial levels (E_i), spin assignments of initial and final levels (J_i^π, J_f^π), γ-ray energies E_γ, relative intensities I_γ, DCO ratios $R_{\rm DCO}$, IPDCO and assigned multipolarity obtained in the present work. New transitions observed in this work are marked with * while tentative transitions are placed inside parentheses.

E_i(keV)[a]	$J_i^\pi \rightarrow J_f^\pi$	E_γ (keV)[a]	I_γ[b]	$R_{\rm DCO}$	IPDCO	Multipolarity
4526.3(2)	$\rightarrow 13^+$	74.0(1)*	17(2)			
4537.4(3)	$14^+ \rightarrow 13^+$	85.8(4)*	11(1)			$(M1+E2)$
2974.3(2)	$10^+ \rightarrow 8^+$	134.1(1)*	3.0(3)	0.88(15)		$(E2)$
2727.7(3)	$7^{(-)} \rightarrow 6^{(-)}$	139.3(1)*	2.6(3)	0.95(14)[c]		$M1+E2$
2989.1(3)	$8^+ \rightarrow 8^+$	149.6(1)	1.1(3)			$(M1+E2)$
2384.6(2)	$4^- \rightarrow 5^-$	167.6(1)	2.7(3)	0.71(3)[c]		$M1+E2$
3841.2(2)	$11^{(+)} \rightarrow 10^+$	176.4(1)*	6.2(3)	0.65(16)		$M1+E2$
4634.3(3)	$14^{(+)} \rightarrow 13^+$	182.2(1)*	3.0(3)	0.50(1)		$M1+E2$
2588.4(3)	$6^{(-)} \rightarrow 4^-$	204.0(1)*				
2974.3(2)	$10^+ \rightarrow 8^+$	208.6(1)	240(19)	0.89(1)	0.16(3)	$E2$
3986.1(3)	$\rightarrow 11^-$	220.3(2)*	0.8(3)			
2989.1(3)	$8^+ \rightarrow 8^+$	223.5(2)	26(3)	0.92(12)		$M1+E2$
4433.7(2)	$12^{(-)} \rightarrow 12^{(-)}$	255.3(1)*	2.6(2)	1.03(6)		$M1+E2$
2384.6(4)	$4^- \rightarrow 3^+$	256.2(2)	4(1)			$E1+(M2)$
2496.6(2)	$7^- \rightarrow 5^-$	278.4(1)	3.5(3)	0.93(17)		$E2$
2800.5(2)	$7^{(-)} \rightarrow (6^-)$	285.4(1)	3.2(3)	1.18(20)[c]		$M1+E2$
2811.1(2)	$7^- \rightarrow (6^-)$	296				
2515.1(2)	$(6^-) \rightarrow 5^-$	297.5(1)	35(5)[d]	0.87(2)[c,d]		$M1+E2$
3218.8(2)	$\rightarrow 7^+$	317.4(1)*				
3196.8(2)	$9^+ \rightarrow 8^+$	357.1(1)	23(2)	0.56(12)	−0.10(4)	$M1(+E2)$
2588.4(3)	$6^{(-)} \rightarrow 5^-$	370.8(1)	10.8(8)	1.00(6)[c]		$M1+E2$
2384.6(4)	$4^- \rightarrow 4^+$	371.7(1)		0.83(8)		$E1+(M2)$
6076.4	$\rightarrow 15^{(+)}$	(383)				
2775.8(2)	$(5^-) \rightarrow 4^-$	391.2(1)*	2.6 (2)			$(M1+E2)$
4159.3(3)	$12^- \rightarrow 11^-$	393.5(1)*	8(1)	0.71(42)	−0.18(2)	$M1(+E2)$
4588.2(3)	$13^- \rightarrow 12^{(-)}$	410.2(2)				$(M1+E2)$
4178.2(2)	$12^{(-)} \rightarrow 11^-$	412.4(1)	35(2)[d]	0.71 (2)[d]		$M1+E2$
1776.0(2)	$6^+ \rightarrow 4^+$	414.7(1)	829(94)	1.05(1)	0.10(1)	$E2$
2811.1(2)	$7^- \rightarrow 6^+$	415.0(1)				
5536.6(3)	$16^+ \rightarrow 15^+$	441.8(1)	10(1)	0.58(9)	−0.08(4)	$M1(+E2)$
4140.1(2)	$12^+ \rightarrow 12^+$	452.5(1)	26(2)	0.96(3)	0.24(3)	$M1+E2$
5094.8(3)	$15^+ \rightarrow 14^{(+)}$	461.4(2)	12(1)	0.56(1)		$M1+E2$
4946.8(4)	$13^{(+)} \rightarrow 12^+$	475.7(1)*	10(3)	0.54(21)		$M1+E2$
4663.2(4)	$(13^-) \rightarrow 12^{(-)}$	485.0(3)*	4.2(3)			$(M1+E2)$
3709.7(2)	$10^- \rightarrow 9^-$	516.1(1)	25(3)	0.72(10)[c]	−0.03(4)	$M1(+E2)$
3716.8(5)	$(10^-) \rightarrow 9^-$	523.2(4)*	14(1)	0.94(4)[c]		$M1+E2$
3940.6(3)	$(11^-) \rightarrow 9^-$	524.0(2)*	12(1)			$(E2)$
5114.6(3)	$15^- \rightarrow 13^-$	526.4(1)	10(1)	1.10(1)		$E2$
4946.8(4)	$13^{(+)} \rightarrow 12^{(+)}$	529.5(1)*	7(1)	0.75(12)		$M1+E2$
3716.8(5)	$(10^-) \rightarrow (8^-)$	544.8(5)*	4.4(4)			$(E2)$
5429.3	$(14^+) \rightarrow 13^{(+)}$	(548)				
4726.8(2)	$13^{(-)} \rightarrow 12^{(-)}$	548.6(1)	11(1)	0.70(3)		$M1+E2$
5141.0(3)	$14^{(-)} \rightarrow 13^-$	552.8(2)*	6.5(3)	0.71(5)		$M1+E2$
3070.5(3)	$8^{(-)} \rightarrow (6^-)$	555.3(1)	11(1)	2.04(30)[c]		$(E2)$
5094.8(3)	$15^+ \rightarrow 14^+$	557.3(1)	40(3)	0.66(4)	−0.05(6)	$M1(+E2)$
2781.2(2)	$6^- \rightarrow 5^-$	563.6(1)	13(1)	1.10(6)[c]	−0.17(12)	$M1(+E2)$
4082.7	$\rightarrow 8^{(-)}$	(572)				
3765.8(2)	$11^- \rightarrow 9^-$	572.2(1)	159(12)	1.05(3)	0.08(2)	$E2$
3070.5(3)	$8^{(-)} \rightarrow 7^-$	573.9(2)	22(2)			$(M1+E2)$
5114.6(3)	$15^- \rightarrow 14^+$	576.7(3)	4.6(3)	0.70(8)		$E1$
4417.5(2)	$12^{(+)} \rightarrow 11^+$	579.8(1)*	12.1(6)	0.50(2)		$M1+E2$
5033.(4)	$14^+ \rightarrow 13^+$	581.0(3)*	9.99(66)	0.69(12)	−0.07(1)	$M1(+E2)$
2811.1(2)	$7^- \rightarrow 5^-$	593.5(1)	106(10)	0.95(3)	0.08(1)	$E2$
3570.6(2)	$10^+ \rightarrow 10^+$	596.3(1)*	22(2)	1.40(10)	0.09(1)	$M1+E2$

TABLE I. (*Continued.*)

E_i(keV)[a]	$J_i^\pi \rightarrow J_f^\pi$	E_γ (keV)[a]	I_γ[b]	$R_{\rm DCO}$	IPDCO	Multipolarity
3407.1	$\rightarrow 7^-$	(596)				
5696.1(4)	$16^{(+)} \rightarrow 15^+$	601.3(2)*	32(3)			$(M1+E2)$
5034.9(2)	$\rightarrow 12^{(-)}$	601.2(1)*	1.2(1)			
3193.4(3)	$(7^-) \rightarrow 6^{(-)}$	605.0(1)*				
3416.6(2)	$9^- \rightarrow 7^-$	605.5(1)*	63(3)	1.90(29)[c]	0.40 (1)	$E2$
5240.6(4)	$(15^+) \rightarrow 14^{(+)}$	606.3(2)*	5.2(7)			$(M1+E2)$
2396.3(2)	$6^+ \rightarrow 6^+$	620.3(2)	22(2)	0.99(13)	0.10(2)	$M1+E2$
4471.1(4)	$12^+ \rightarrow 11^+$	633.4(3)*	12(4)	0.59(12)	−0.21(6)	$M1(+E2)$
3449.2(2)	$8^{(-)} \rightarrow 7^-$	638.1(1)*	22(2)	0.67(4)		$M1+E2$
3709.7(2)	$10^- \rightarrow 8^{(-)}$	638.9(1)	16(1)	1.12(7)	0.22 (4)	$E2$
3837.7(2)	$11^+ \rightarrow 9^+$	(641)				
2012.6(3)	$4^+ \rightarrow 4^+$	651.8(1)	6.0(7)		0.09(7)	$M1+E2$
3171.6(2)	$(8^-) \rightarrow (6^-)$	656.5(1)	14(2)			$(E2)$
666.3(1)	$2^+ \rightarrow 10^+$	666.3(1)[e]	1000	1.24(1)		$E2$
3171.6(2)	$(8^-) \rightarrow 7^-$	674.8(1)	13(2)	0.87(1)[c]		$M1+E2$
3496.4(2)	$8 \rightarrow 7^-$	685.3(1)*	11(1)	0.80(8)[c]		
3664.8(2)	$10^+ \rightarrow 10^+$	691.2(2)*	15(1)			$(M1+E2)$
1361.3(1)[f]	$4^+ \rightarrow 2^+$	695		0.91(1)	0.09(1)	$E2$
3193.6(2)[f]	$9^- \rightarrow 7^-$	697		1.45(1)[c]	0.13(1)	$E2$
4116.6	$\rightarrow 9^-$	(700)				
2128.6(3)	$3^+ \rightarrow 2^+$	708.2(1)				$M1+E2$
3687.6(2)	$12^+ \rightarrow 10^+$	713.4(1)	158(12)	1.01(3)	0.11(2)	$E2$
2496.6(2)	$7^- \rightarrow 6^+$	720.5(1)	315(28)	0.70(1)	0.05(1)	$E1(+M2)$
4433.7(2)	$12^{(-)} \rightarrow 10^-$	724.0(1)	11 (1)	1.96(32)[c]		$E2$
3570.6(2)	$10^+ \rightarrow 8^+$	730.6(2)*	11(1)	1.00(30)	0.03(1)	$E2$
4881.3(2)	$13^{(+)} \rightarrow 12^+$	741.2(1)*	9(1)	0.39(13)		$M1+E2$
5469.3(3)	$15^{(-)} \rightarrow 13^{(-)}$	742.5(2)*	6(1)	0.95(11)		$(E2)$
5164.5	$\rightarrow 12^{(+)}$	(747)				
1420.4(1)	$2^+ \rightarrow 2^+$	754.1(1)	20(4)	1.05(13)	0.17 (3)	$M1+E2$
4452.3(2)	$13^+ \rightarrow 12^+$	764.7(1)	53(4)	0.50(7)	−0.02(1)	$M1(+E2)$
3496.4(2)	$8 \rightarrow 6^+$	792.7(2)*				
3319.8(2)	$\rightarrow (6^-)$	804.7(1)*	3.6(3)			
4010.9(2)	$10^+ \rightarrow 9^+$	814.1(1)*	8(2)	0.46(4)	−0.27(18)	$M1(+E2)$
4588.2(3)	$13^- \rightarrow 11^-$	822.4(1)	34(3)	1.2(2)	0.05(4)	$E2$
3646.4(3)	$9^{(-)} \rightarrow 7^-$	835.3(2)*	22(2)	1.02(14)		$(E2)$
4611.8(2)	$13^{(-)} \rightarrow 11^-$	846.0(1)	15(1)	1.64(25)[c]		$(E2)$
4537.4(3)	$14^+ \rightarrow 12^+$	849.8(1)	41(5)	0.93(3)	0.20(13)	$E2$
2217.6(2)	$5^- \rightarrow 4^+$	856.3(1)	241(20)	0.78(3)	0.04(3)	$E1+M2$
3837.7(2)	$11^+ \rightarrow 10^+$	863.4(1)	27(3)	0.51(8)	−0.06(1)	$M1(+E2)$
4085.8(4)	$11^{(+)} \rightarrow 9^+$	889.2(1)*	10 (1)			
3796.4(2)	$8^+ \rightarrow 6^+$	895.0(1)*	9(1)	0.41(8)	−0.11(4)	$M1(+E2)$
3664.8(2)	$10^+ \rightarrow 8^+$	899.2(1)*	19(1)	0.94 (6)	0.08 (4)	$E2$
2703.7(2)	$6^+ \rightarrow 6^+$	927.7(1)	2.5(3)	1.17(9)	0.29 (13)	$M1+E2$
3452.4(4)	$\rightarrow (6^-)$	937.3(3)*				
4143.3(2)	$(11^+) \rightarrow 9^+$	946.5(1)*	3.2(3)			$(E2)$
6060.9(3)	$17^- \rightarrow 15^-$	946.3(1)	5(1)	1.10(2)	0.20(10)	$E2$
4634.3(3)	$14^{(+)} \rightarrow 12^+$	946.7(1)	34(3)	1.02(5)		$(E2)$
5088.7(2)	$\rightarrow 12^+$	948.6(1)*				
2729.0	$\rightarrow 6^+$	(953)				
3474.6(2)	$\rightarrow (6^-)$	959.5(1)*	1.70(16)			
5140.3(3)	$14^- \rightarrow 12^{(-)}$	962.1(2)	16(1)	1.22(9)	0.20(7)	$E2$
2765.6(2)	$8^+ \rightarrow 6^+$	989.6(1)	334(69)	1.10(2)	0.12(1)	$E2$
3510.7(2)	$8^{(-)} \rightarrow 7^-$	1014.1(1)*	41(3)	0.70(4)		$(M1+E2)$
3916.0(2)	$\rightarrow 7^+$	1014.6(1)*				
2396.3(2)	$6^+ \rightarrow 4^+$	1035.2(2)	17(2)	1.12(12)	0.04(1)	$E2$
2831.0	$\rightarrow 6^+$	(1055)				

TABLE I. (*Continued.*)

E_i(keV)[a]	$J_i^\pi \rightarrow J_f^\pi$	E_γ (keV)[a]	I_γ[b]	$R_{\rm DCO}$	IPDCO	Multipolarity
5696.1(4)	$16^{(+)} \rightarrow 14^{(+)}$	1062.2(2)	11(8)	0.91(37)		$(E2)$
2839.7(2)	$8^+ \rightarrow 6^+$	1063.7(1)	52(7)	0.94(7)	0.07 (3)	$(E2)$
3837.7(2)	$11^+ \rightarrow 8^+$	(1072)				
4085.8(4)	$11^{(+)} \rightarrow 10^+$	1111.5(3)*	11(1)	0.35(10)		$M1+E2$
2901.4(2)	$7^+ \rightarrow 6^+$	1125.4(1)*	13(2)	0.56(5)	−0.06(1)	$M1(+E2)$
5693.6(5)	$15^{(+)} \rightarrow 14^+$	1156.2(2)*	4(1)	0.70(18)		$(M1+E2)$
2968.2(3)	$7^{(+)} \rightarrow 6^+$	1192.2(2)*	7(1)	0.76(10)		$(M1+E2)$
2989.1(3)	$8^+ \rightarrow 6^+$	1213.5(1)	11.0(6)	1.14(8)		$E2$
3013.8(3)	$(8^+) \rightarrow 6^+$	1237.8(2)*	4.2(8)			$(E2)$
4149.1(2)	$\rightarrow 7^+$	1247.7(1)*				
3763.0(3)	$(9^-) \rightarrow 7^-$	1266.4(2)*	6(2)			$(E2)$
3064.6(2)	$7^{(+)} \rightarrow 6^+$	1288.6(1)*	10(2)	0.48(6)		$M1+E2$
2012.6(3)	$4^+ \rightarrow 2^+$	1346.3(3)	8(2)	1.01(30)		$E2$
4341.3(2)	$11^{(+)} \rightarrow 10^+$	1367.0(1)*	4.4(3)	0.54(8)		$M1+E2$
2128.6(3)	$3^+ \rightarrow 2^+$	1462.3(3)	6.1(8)			$(M1+E2)$
5163.9(3)	$(13^+) \rightarrow 12^+$	1476.3(2)*	3.2(4)			$(M1+E2)$
2183.8(1)	$2^+ \rightarrow 2^+$	1517.5(1)	3(1)			$(M1+E2)$

[a]Level energies have been determined using the centroid of the most intense γ ray decaying from that level. Reported uncertainties in γ-ray energies have been obtained by least-squares peak fitting.
[b]Intensities have been measured relative to the 666.3-keV γ transition with $I_\gamma = 1000$.
[c]DCO ratios obtained from a dipole ($E1$) gate.
[d]Intensity and DCO ratio of transition also included the contributions from the 296.0-keV transition (for the 297.5-keV transition) and 410.2-keV transition (for the 412.4-keV transition).
[e]Centroid was measured from total projection spectrum.
[f]Uncertainty of 0.1 keV has been assumed for the decaying transition as centroid measurement was not possible due to the presence of another transition with overlapping energy.

A. Positive-parity structures

The yrast band G is well established from previous works [26–28] and has been verified in our work along with the addition of new transitions decaying to this structure. Several high-energy γ rays have been observed in the 666-695 and 666-415 double gates (Fig. 5) and have been placed to decay to the 1776.0-keV level. These transitions and corresponding levels have been grouped in the level scheme as "L" but they have not been identified as part of any band structure (Fig. 3). This group includes the 1192.2-, 1237.8-, 1288.6-, and 1125.4-keV transitions (Figs. 5 and 6). The 317.4-, 1014.6-, 895.0-, and 1247.7-keV transitions have been observed in coincidence with the 1125.4- and 414.7-keV γ rays (Fig. 6). Another newly observed γ ray of energy 1367.0 keV decays to the 10^+ level of the yrast band.

Structure P3 is based on the 4140.1-keV level that decays to the 12^+ level of the yrast band via the 452.5-keV transition. Two new γ rays were observed in the 452.5-713.4 double gate. The 741.2- and 948.6-keV transitions have been placed parallel to each other. This placement has been confirmed via the 741.1-948.6 double gate where the 452.5- and 713.4-keV transitions were not observed. The 3664.8-keV level (below structure P3) was established with 899.2- and 691.2-keV transitions feeding into the 8^+ and 10^+ levels of the positive-parity yrast band. A 176.4-keV γ ray was also observed to decay to this level.

The 3837.7-keV level in structure P2 decays to the 10^+ state of the ground band via the 863.4-keV transition [28]. A cascade of two γ rays of energies 529.5 and 579.8 keV (Fig. 7) have been observed to decay to this level, extending this structure to 4946.8 keV. This level features another decay path via the 475.7- and 633.4-keV transitions which feed into the 3837.7-keV level of the same structure. The 4452.3-keV level was established in a previous work [27]. Two more γ rays having energies 581.0 and 74.0 keV have been observed to decay to this level. An 85.8-keV transition decays from the 14^+ level of the yrast band to this level. The 596.3-keV transition (below P2) was observed in the 208.6-989.6 double gate and was placed above this cascade, decaying into the 10^+ level.

The previously observed cascade (structure P1) consisting of the 1063.7- [$R_{\rm DCO} = 0.94$ (7)] and 357.1-keV [$R_{\rm DCO} = 0.56$ (12)] transitions feeding into the 6^+ state of the yrast band has been observed and verified in our work. An earlier work [29] had assigned a spin value of $(6)^+$ to the 2839.7-keV level of this cascade and also observed a 1476.2-keV γ ray decaying in parallel to the 1064.1-keV transition from the same level. This transition, however, is not observed in the current work. We have observed a 134.1-keV transition with an $R_{\rm DCO}$ value of 0.88 (15) feeding into this level from the 10^+ level of the yrast band. The IPDCO values for the 1064.1- and 356.1-keV transitions indicate multipolarities $E2$ and $M1(+E2)$ for these transitions, respectively. Owing to these observations, the 2839.7-keV level has been assigned a spin-parity 8^+ and the 3196.8-keV level above it was assigned 9^+. A 730.6-keV γ ray was observed to feed into the 2839.7-keV level while a 946.5-keV transition feeds into the

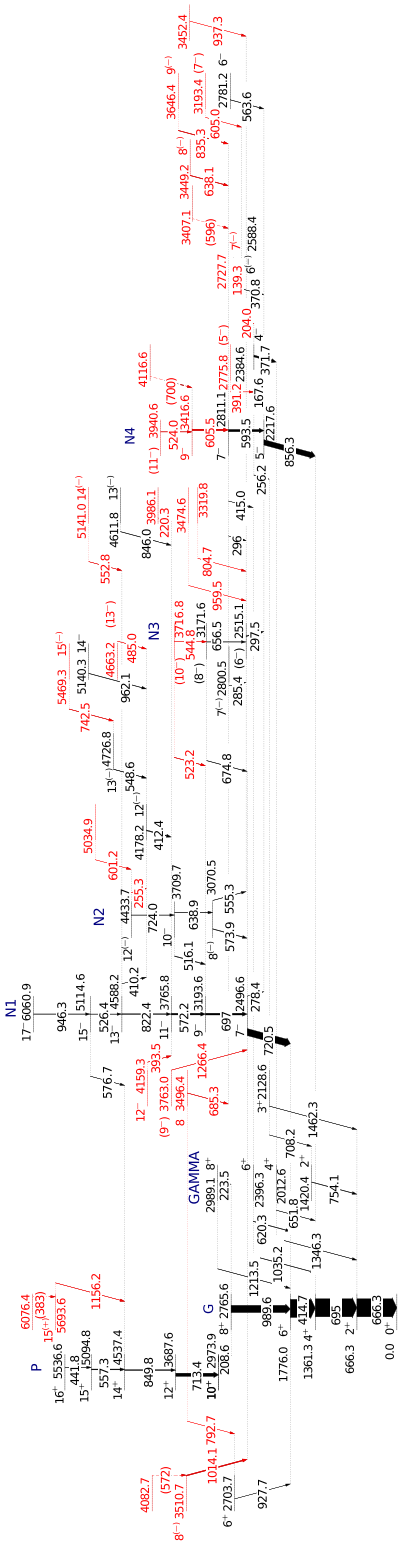

FIG. 4. The negative-parity section of the level scheme for ^{126}Te as obtained in the present work. The new γ rays and levels are marked in red.

3196.8-keV level. Additionally, a new transition of energy 814.1 keV was observed to decay to the 3196.8-keV level, extending this cascade to a spin value of 10^+ (Fig. 8).

A new level having energy 4085.8 keV has been established with two γ rays having energies 1111.5 and 889.2 keV, decaying to the yrast 10^+ level and the 9^+ level of structure P1, respectively. While DCO and IPDCO measurements for the 889.2-keV transition were not possible, a DCO value of 0.35(10) for the 1111.5γ ray led to an assignment of $11^{(+)}$ for this level. The 4634.3- and 5696.1-keV levels were established in a previous work [27] with a 461.4-keV γ ray feeding into the 4634.3-keV level from the yrast 15^+ level (energy 5094.8 keV, also established in the same work). We have observed a 601.3-keV transition in coincidence with the 557.3- and 849.8-keV γ rays. The 601.3-keV γ ray is not present in the 1062.5-964.7 double gate, indicating that this transition is in parallel with the 1062.5-keV transition. Subsequently, the 601.3-keV transition was placed between the 5696.1- and 5094.8-keV levels. The 1476.3-keV γ ray was observed (weakly) in the 713.4-208.6 double gate. As this transition was not present in the 713.4-849.8 double gate, we have placed this transition to decay to the 3687.6-keV level.

The band labeled "GAMMA" was reported to be the favored partner of the $K = 2$ quasi-γ band [30]. This band has been observed and verified in our work. However, owing to poor statistics, this band could not be extended to higher spins, nor were any other transitions observed decaying to this structure. Thus, its signature partner could not be established.

B. Negative-parity structures

The negative-parity bands N1 and N2 were established in earlier works and identified as signature partners, as indicated by the energy staggering [28]. The same has been verified in our work and further enriched with the addition of several transitions decaying to the levels of these structures, with a modification in the placement of the 962.1-keV γ ray. This transition was previously placed in parallel to the 412.4-keV γ ray, decaying to the 3765.8-keV level [27]. The 572.2-695 double gate shows the presence of both the 412.4- and 962.1-keV transitions (Fig. 9) and the 412.4-962.1 double gate shows the presence of the 572.2-keV γ ray as well as the rest of the transitions in that cascade. A 255.3-keV transition has been observed in the 412.4-572.2 double gate(Fig. 9) and hence placed above this cascade, feeding into the 4178.2-keV level. The 255.3-412.4 double gate, however, does not show the presence of the 962.1-keV transition. Hence, the 255.3- and 962.1-keV γ rays have been placed parallel to each other, with the 962.1-keV transition placed above the 412.4-keV γ ray. Another transition of energy 485.0 keV was found to decay to the 4178.2-keV level. A newly observed 1014.1-keV transition feeds into the 2496.6-keV level of band N1 (Fig. 4, leftmost side) while another new transition of energy 220.3 keV (placed near structure N3), decays to the 3765.8-keV level of the same band.

A 552.8-keV γ ray decays to the 4588.2-keV level of N1. A DCO value of 0.71 indicated a dipole-type transition. The 1266.4-keV transition has been (weakly) observed in the 720.5-414.7 double gate and feeds into the 7^- level of structure N1 while the 393.5-keV γ ray feeds into the 11^- level of the same structure. Owing to very low statistics, the

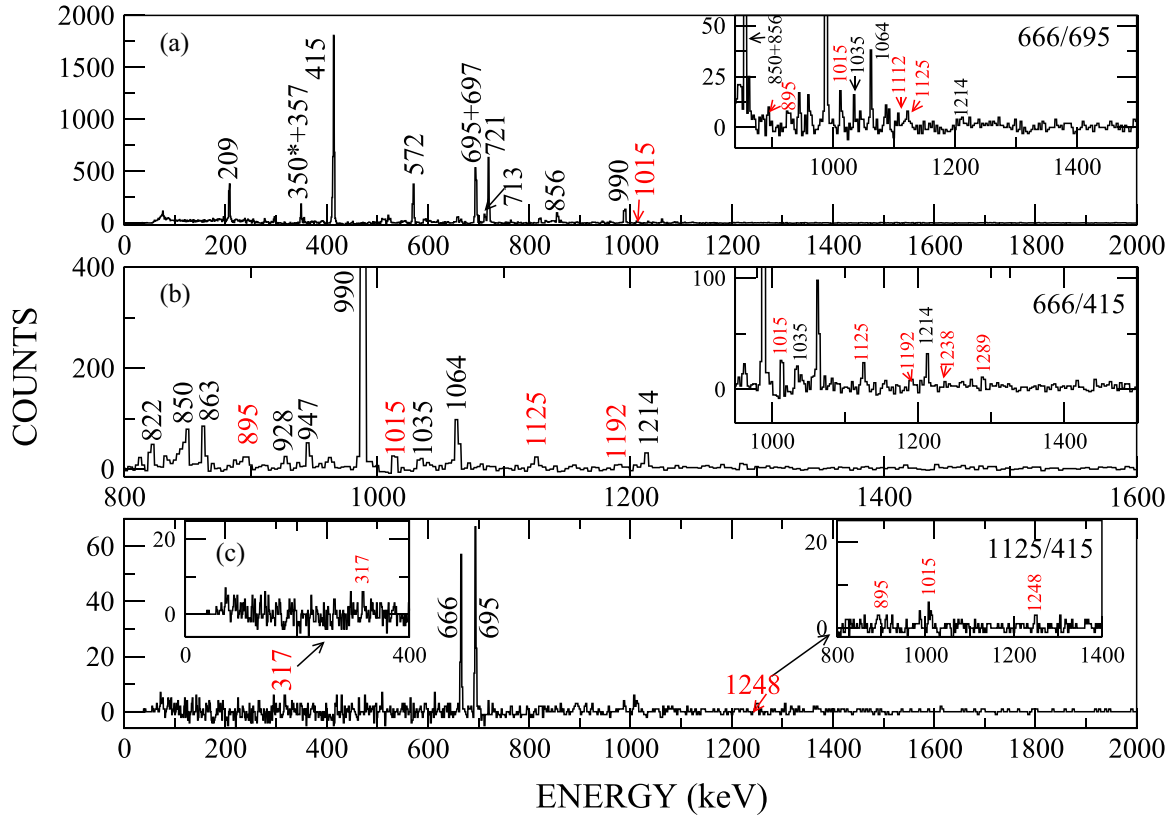

FIG. 5. Spectra obtained from the γ-γ-γ cube showing some of the transitions decaying to the yrast band. These transitions are placed in the positive-parity part of the level scheme. New transitions are marked in red. Panel (a) is a double gate on the 666- and 695-keV γ rays. The transition marked '*' is from ^{125}Te, which was also populated in this experiment. Panel (b) is the double gate 666/415 keV, and panel (c) is the double gate 1124/415. Insets have been employed to indicate the new (weaker) transitions more clearly. (γ-ray energies have been rounded off to the nearest integer.)

R_{DCO} and ΔIPDCO for the 1266.4-keV γ ray could not be measured, and the spin-parity for this level is tentative.

A 742.5-keV γ ray feeds into the 4726.8-keV level. This level was established earlier [27] with the 548.6-keV transition decaying to the 4178.2-keV level.

The structure N3 based on the 2515.1-keV level was previously known up to the 3171.6-keV level. The placement of the 544.8-keV transition extends this structure to an energy of 3716.8 keV. Two more γ rays of energies 804.7 and 959.5 keV feed into the 2515.1-keV level of the structure which have not been identified with any band structure. Two γ rays of energies 674.8 and 523.2 keV decay from the 3171.6- and 3716.8-keV levels of N3, respectively, to the 2496.6- and 3193.6-keV levels of band N2, respectively. These two transitions were determined to be of a dipole nature and the spin-parity for the levels of N3 were assigned accordingly. Additionally, a 555.3-keV transition decays from the 3070.5-keV level of N2 to the 2515.1-keV level of N3. This transition was determined to be quadrupole in nature.

The placement and nature of the 674.8- and 555.3-keV transitions have resulted in a reevaluation of the spin assignment of the 2515.1-keV level to (6^-) instead of 5^- [29]. The justifications for this spin assignment are as follows:

(i) The 555.3-keV transition, decaying from the 3070.5-keV level of structure N2 has been determined to be of a quadrupole nature from its DCO ratio (Table I). Another transition having energy 573.9 keV decays to the 2496.6-keV level of N1. While DCO measurement for this gamma was not possible in the present work, it has been assigned dipole nature in literature [29]. The observation of both these γ rays resulted in the assignment of a spin value of $8^{(-)}$ to this level. The quadrupole nature of the 555.3-keV transition necessitates a spin assignment of 6^- to the 2515.1-keV level.

(ii) The DCO ratio of the 297.5-keV (296.0-keV) transition(s) is 0.87(2) in the 856.3-keV gate. While this gate has contributions from both the 297.5- and 296.0-keV transitions (the 297.5-keV transition being more intense), the average DCO for both the γ rays comes out to be of dipole nature, contradicting the unstretched transition assignment for the 297.5-keV γ ray [29].

(iii) A 739.18-keV transition of $E1$ nature has been reported [29] to decay from this level to the 1776.0-keV level of the ground band, which would justify the 5^- spin assignment of the 2515.1-keV level. This transition, however, has not been observed in our work.

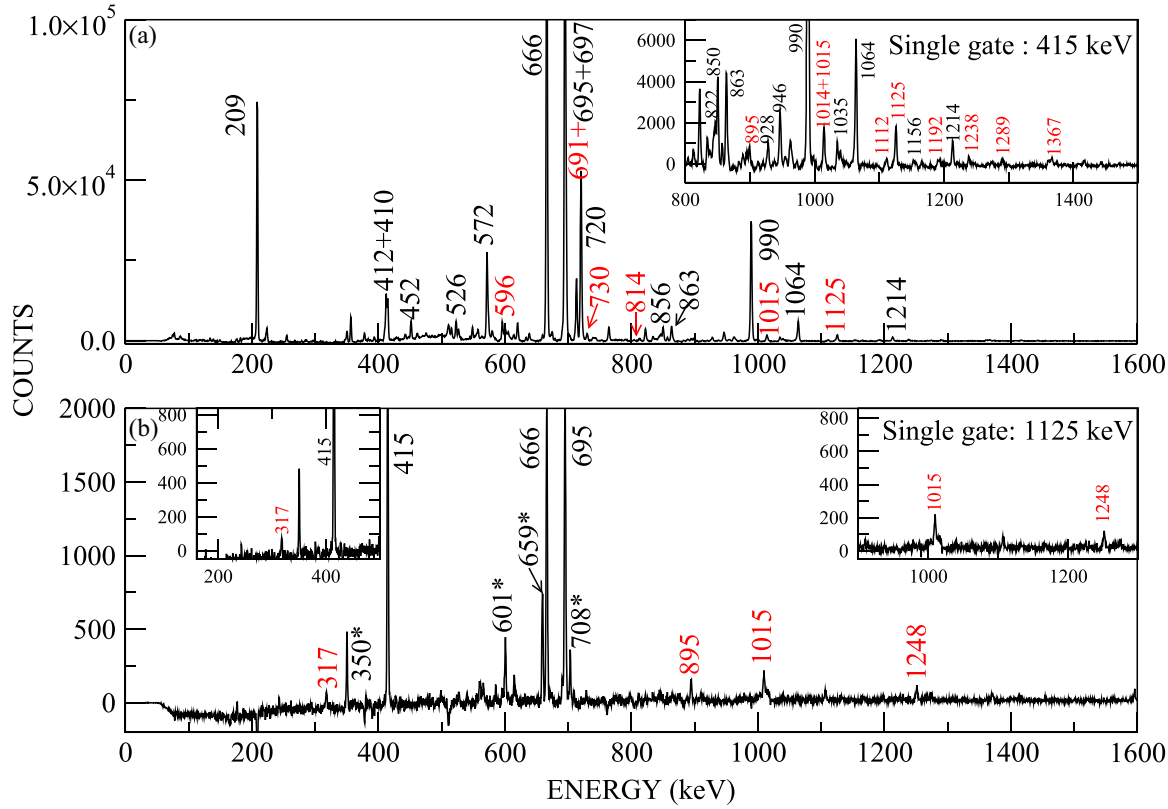

FIG. 6. Spectra obtained from the γ-γ symmetric matrix showing some of the transitions decaying to the yrast band. These transitions are placed in the positive-parity part of the level scheme. Transitions marked with '*' are from ^{125}Te, which was also populated in this experiment. New transitions are marked in red. Panel (a) shows a single-gated spectrum on the 414.7-keV transition. Panel (b) is a single-gate on the 1125.4-keV γ ray. (γ-ray energies have been rounded off to the nearest integer.)

Hence, changing the spin assignment of this level to 6^- is consistent with our observations in the present work.

The structure N4 has similarly been extended with the placement of the 605.5-keV and 524.0-keV transitions above the 2811.1-keV level. Three new transitions, having energies 638.1, 685.3, and 835.3 keV, also decay to the 2811.1-keV level. A γ ray of energy 792.7 keV decays to the 2703.7-keV (6^+) level, in parallel to the 685.3-keV transition, both decaying from the same 3496.4-keV level. The presence of the 167.6-keV γ ray decaying to the 2217.6-keV level has been verified in our work with the addition of another transition of energy 391.2 keV to this cascade. Additionally, several new transitions have been observed that decay to the various levels of N4. These γ rays, however, could not be placed in any structure.

V. DISCUSSION

The low-spin level structure of even-even Te is characterized by equidistant levels corresponding to the consecutive phonon states. The degeneracy of the two-phonon and higher states is usually removed by the residual interactions and has been observed in Te isotopes of mass $A = 118$–130 [26]. The higher spin states are expected to show quasiparticle excitations, and a transition from a vibrational to a possible rotational structure has been reported in several Te isotopes [31,32].

The study of ^{126}Te in earlier works [26–28] extended the level scheme to an energy $\approx$6 MeV. The presence of two-neutron quasiparticle states involving $(h_{11/2}d_{3/2})$ and $(h_{11/2}s_{1/2})$ was proposed, namely, for the 7^- and 5^- states, respectively [26]. A new negative-parity sequence (N2) was observed to decay to the well-established negative-parity band N1 [28]. This structure, N2, was suggested to be the signature partner of the band N1. An interpretation of the states in the CNS and CNSB models indicated that the $\nu(gsd)^{17}_{\pm1/2}(h_{11/2})^7_{1/2}$ is favored at lower spins while $\nu(gsd)^{17}_{\pm1/2}(h_{11/2})^7_{-1/2}$ is favored at high spins. The observation of signature splitting in these bands suggested the presence of triaxiality [28]. The band labeled "GAMMA" had been identified as the favored partner of the $K = 2$ quasi-γ band. Such bands have been observed in even Te isotopes [23,30], the presence of which indicates a deviation from axial symmetry. The transition $4^+_2 \rightarrow 2^+_1$, which is not allowed in the vibrational and γ- unstable models [33], has been observed.

Shell-model calculations were performed using the code ANTOINE [34], which performs large-scale shell-model calculations based on the Lanczos algorithm. The Z50.bonna two-body interaction, which corresponds to the $Z = 50$, $N = 82$ space was used. The valence spaces for both the

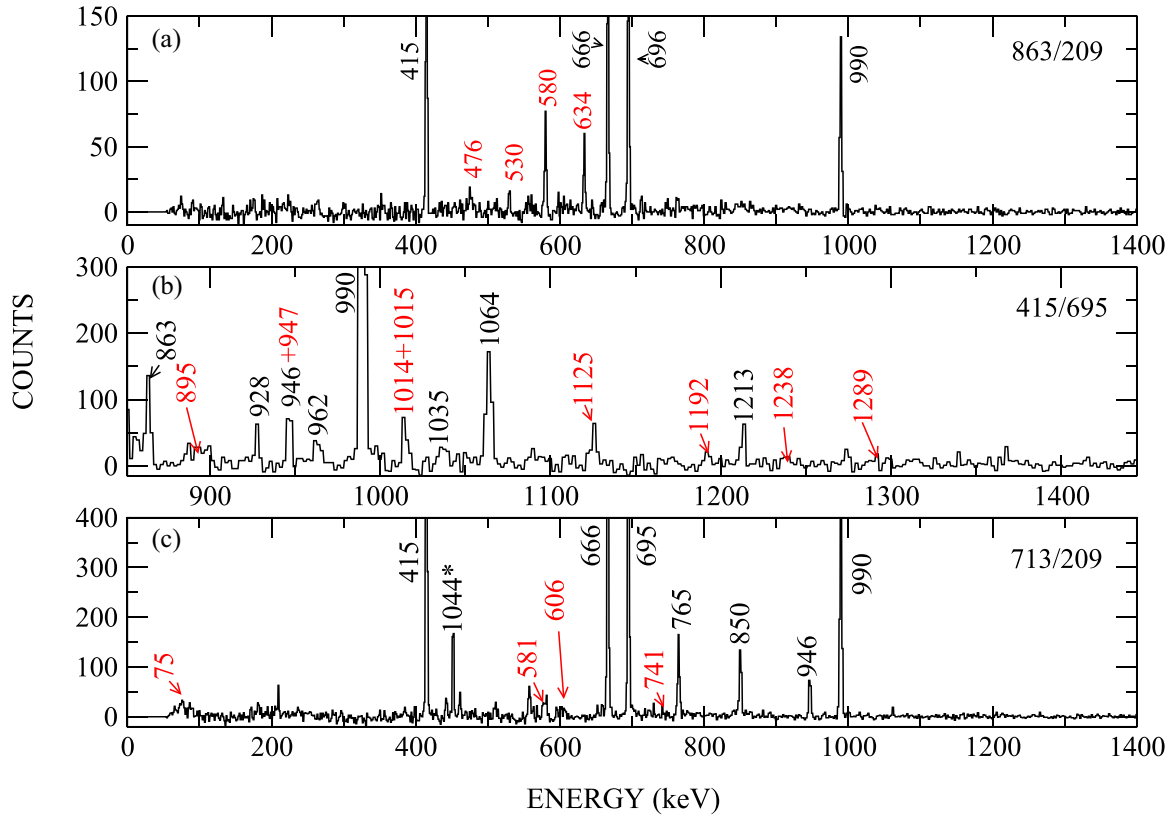

FIG. 7. Spectra obtained from the γ-γ-γ cube with double gates showing some of the prominent transitions observed in coincidence. These transitions are placed in the positive-parity part of the level scheme. New transitions are marked in red. Transitions marked with "*" are from ^{125}Te, which was also populated in this experiment. Panel (a) is a double gate on the 863- and 209-keV γ rays, panel (b) is the double gate 415-695 keV, and panel (c) is the double gate 713-209. Panel (b) has been zoomed in to show the high-energy transitions prominently. (γ-ray energies have been rounded off to the nearest integer.)

protons and neutrons were identical, consisting of the shells $g_{7/2}$, $d_{5/2}$, $d_{3/2}$, $s_{1/2}$, and $h_{11/2}$. The single-particle energies were 0.09320, 0.0, 1.52846, 1.44458, and 2.32997 MeV, respectively. As the dimensions of the resulting matrices were too large to consider the whole space for calculating the wave functions, the truncations were chosen to allow a maximum of eight neutrons in the $\nu h_{11/2}$ shells and a maximum of two protons in the $\pi h_{11/2}$. Truncations were chosen to reproduce the experimental energy levels optimally. A comparison between the shell-model calculations and some of the experimental energy levels is shown in Fig. 10, and the composition of the wave functions are listed in Table II.

For the low-spin positive-parity states, the energy differences between the experimental and shell-model energy levels range from 119 keV for the 2_1^+ state to 673 keV for the 8_1^+ state. For higher spin states, this difference is much more pronounced, with the difference being >500 keV for spin values 10^+ onwards. The 2_1^+ state is predicted at 547 keV.

For the negative-parity states, the energy differences between the experimental values and shell-model calculations lie between 58 and 629 keV, respectively. The calculated yrast states lie lower in energy than the experimental levels.

A previous work [35] using the NuShellX code predicted the 2_1^+ state at 548 keV. The differences in energies, between theory and experiment for states up to 6_1^+ differed from 119 to 213 keV. The notable difference arises in the predictions of the states from 8_1^+ onwards, which predict considerably lower values as compared with the calculations obtained in the present work. This can be attributed the modified Hamiltonian used by the authors, which reduced the effect of the $n-n$ part of the effective interaction on the $d_{3/2}$ and $s_{1/2}$ orbitals while keeping the effect on the $g_{7/2}$ and $d_{5/2}$ orbitals unchanged [35].

The Te isotopes with $N \approx Z$ have been found to exhibit strong proton-neutron correlations, which result in a near-collective behavior in these nuclei. However, for the heavier mass Te isotopes, these correlations are considerably reduced, which manifests in a seniority-based coupling [37], and it is the breaking of proton and neutron pairs that results in the generation of the higher spin states. Another aspect of the effective interactions includes the effects of the three-body force on the energy levels [38,39]. The average energy shift from a three-body force is given as $\Delta E = \binom{n}{k} \overline{V_3}$, where n is the number of valence particles and $\overline{V_3}$ is the average value of the diagonal matrix elements of the three-particle states [38]. This force is of a repulsive nature and is expected to be more effective with an increasing number of particles in the $h_{11/2}$ orbital. In the present truncated case, as the occupancy of the $h_{11/2}$ orbital varies from four to six, the magnitude of this force increases five times. This could possibly explain the

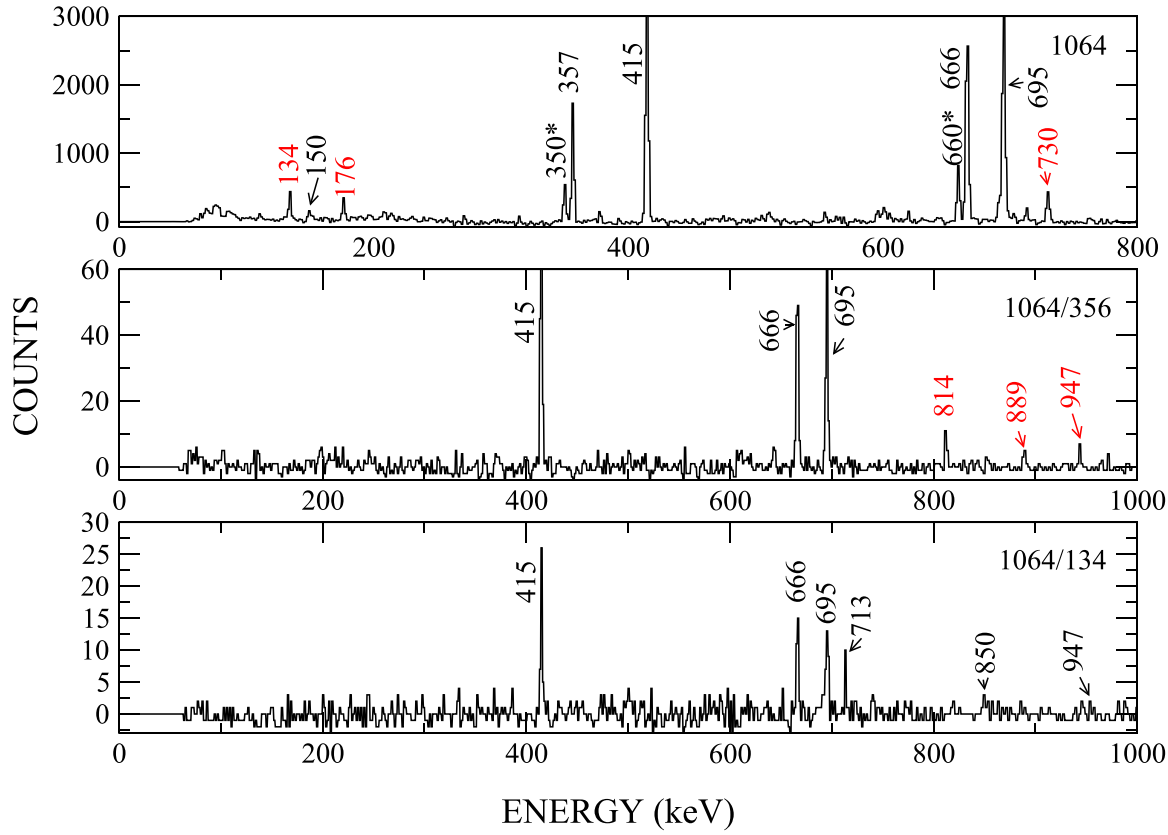

FIG. 8. Spectra obtained from the γ-γ-γ cube with double gates showing some of the prominent transitions observed in coincidence. These transitions are placed in the positive-parity part of the level scheme. Transitions marked with "*" are from ^{125}Te, which was also populated in this experiment. The top panel is the spectrum obtained with a single gate on the 1064-keV transition. The newly observed transitions are marked in red. Both the 730- and 134-keV transitions decay to the 2839.7-keV level of structure P1. The middle panel is the double gate 356-1064. The bottom panel shows a gate on the 1064- and 134-keV transitions. The presence of all the γ rays in this cascade and the absence of the 134-keV transition in the 1064-356 gate justifies the placement of this transition in the level scheme. (γ-ray energies have been rounded off to the nearest integer.)

larger discrepancies in energy levels between the experimental and calculations for higher spins.

In the shell-model picture for yrast states up to 11^+_1, the major contribution comes from the wave functions with $\pi(d_{5/2})^2$ coupled to $\nu(d_{3/2})^4(h_{11/2})^6$. For the 13^+_1 and 15^+_1 states the major contribution comes from $\pi(d_{5/2})^2$ and $\pi(d_{7/2})^1(d_{5/2})^1$ coupled to four neutrons in $h_{11/2}$. The first aligned state occurs at 6^+, which is built by the alignment of the $\pi(g_{7/2})^1(d_{5/2})^1$ protons. The 6^+_2 is predicted at $\approx$1825 keV by SM calculations, while in the experiment, it occurs at 2396 keV. This state is a collective one [28] with the configuration $\pi(d_{5/2})^2 \bigotimes \nu(g_{7/2})^6(d_{5/2})^6(d_{3/2})^4(s_{1/2})^2(h_{11/2})^6$ Another aligned state occurs for 10^+_1 (most probable configuration $\pi(d_{5/2})^2 \bigotimes \nu(g_{7/2})^8(d_{5/2})^6(d_{3/2})^4(s_{1/2})^2(h_{11/2})^4$] where we observe the breaking and alignment of $2h_{11/2}$ neutrons. In Fig. 11, we also observe shallow minima at 6^+_1 and 10^+_1. The large energy gaps after the 6^+_1 and 10^+_1 states may be attributed to the extra energy required to generate the higher angular-momentum states after alignment.

Three new 10^+ states have been observed experimentally at 3664.8, 3570.6, and 4010.9 keV excitation energies, respectively. Corresponding shell-model calculations indicated a highly mixed configuration for the 10^+_2 state, which has the most probable configuration the same as that for 10_1, but accounts for only 9.1% of the total while the 10^+_3 state has the most probable configuration $\pi(g_{7/2})^1(d_{5/2})^1 \bigotimes \nu(g_{7/2})^8(d_{5/2})^6(d_{3/2})^2(s_{1/2})^2(h_{11/2})^6$. Experimentally, we report the three previously unobserved 7^+ states at 2901.4, 2968.2, and 3064.6 keV(Fig. 3). Shell-model calculations predict the 7^+ levels at energies 2198, 2581, and 2871 keV. Most probable configurations for these states are indicated in Fig. 10. The $7^+_{1,3}$ states involve the alignment of the $g_{7/2}$ and $d_{5/2}$ protons while the 7^+_2 state involves the alignment of the $g_{7/2}$ protons.

The first 11^+ state occurs in the experiment at 3837.7 keV. The shell-model calculations predict this state at $\approx$3230 keV. We observed three new 11^+ levels at 3841.2, 4085.8, and 4341.3 keV, respectively. From calculations, we find that the 11^+_1 level involves the alignment of two protons in the $\pi d_{5/2}$ shell and the creation of two neutron holes in $\nu g_{7/2}$ orbital from the excitation of two neutrons to $h_{11/2}$. This state involves the alignment of one neutron hole in $g_{7/2}$ and a particle in $h_{11/2}$. The 13^+_1, 13^+_2, and 13^+_3 states in the experiment

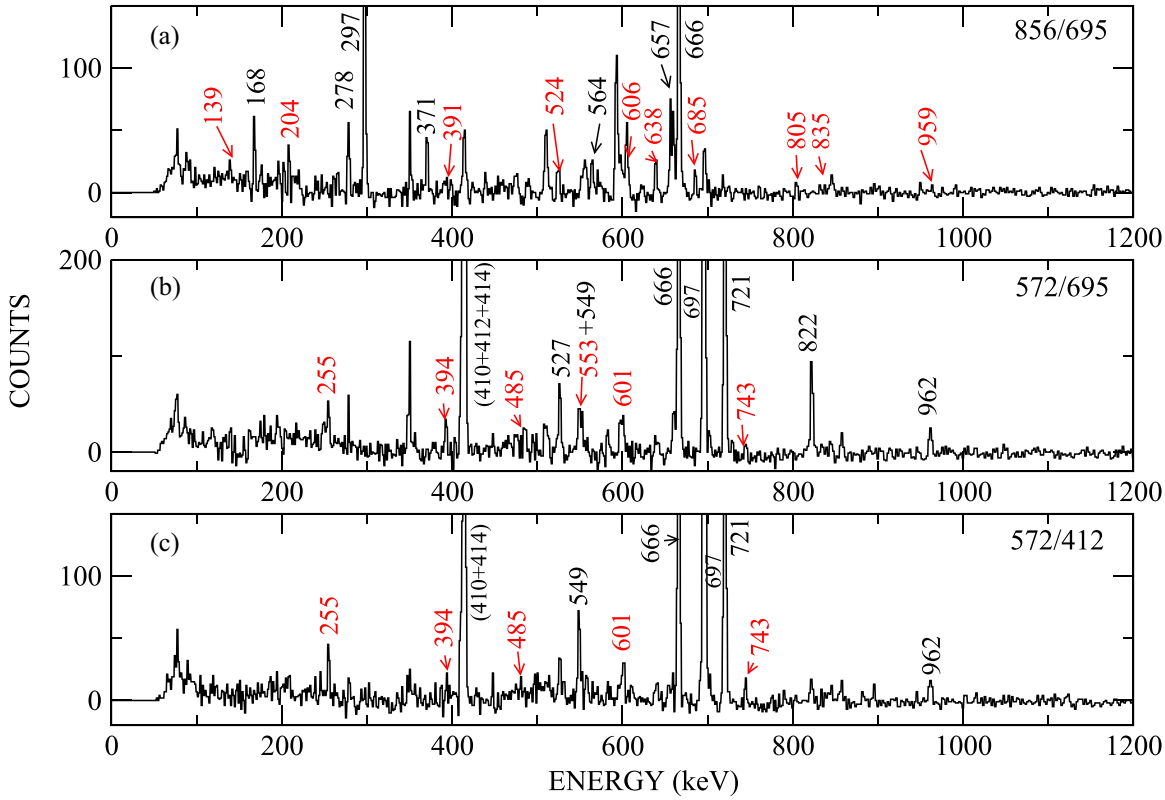

FIG. 9. Spectra obtained with double gates showing some of the prominent transitions observed in coincidence. These transitions are placed in the negative-parity part of the level scheme. New transitions are marked in red. Panel (a) is a double gate on the 856- and 695-keV γ rays, panel (b) is the double gate 572-695, and panel (c) is the double gate 572-412. (γ-ray energies have been rounded off to the nearest integer.)

are at 4452.3, 4881.3, and 4946.8 keV, the latter two have been observed in this work for the first time. While the wave functions of the 13^+_1 and 13^+_3 as predicted by calculations are identical (Table II), the wave function for 13^+_2 involves the coupling of $g_{7/2}$ and $d_{3/2}$ neutrons. Calculations predict these states at 3644 and 3782 keV. The 13^+, 14^+, and 15^+ states have been suggested to involve the breaking of one proton pair and a neutron pair [27]. The shell-model calculations show $\pi(d_{5/2})^2 \bigotimes \nu(g_{7/2})^8(d_{5/2})^6(d_{3/2})^4(s_{1/2})^2(h_{11/2})^4$ to be the most probable configuration for both 13^+ and 14^+ while for the 15^+ state the proton part of the wave function is $\pi(g_{7/2})^1(d_{5/2})^1$.

The lowest observed negative-parity state in the experiment is 5^-. Shell-model calculations indicate the 5^-, 7^-, 9^-, and 11^- states to each have neutron configurations $\nu(d_{3/2})^3(h_{11/2})^5$. The structure N3 is based on the lowest observed 6^- state in experiment, having the most probable configuration $\pi(d_{5/2})^2 \bigotimes \nu(g_{7/2})^8(d_{5/2})^6(d_{3/2})^3(s_{1/2})^2(h_{11/2})^5$ while N4 is based on the lowest observed 5^- state with most probable configuration $\pi(d_{5/2})^2 \bigotimes \nu(g_{7/2})^8(d_{5/2})^6(d_{3/2})^3(s_{1/2})^2(h_{11/2})^5$. The 6^- state involves the coupling of $h_{11/2}$ and $d_{3/2}$ neutrons. Newly observed 8^- states are at 3449.2 and 3510.7 keV in addition to the previously observed 3171.6 keV level. A new 12^- state is observed at 4159.3 keV, while a 14^- state is observed at 5141.0 keV. All these states involve the coupling of an $h_{11/2}$ neutron with either a $d_{3/2}$ neutron (8^-_2, $12^-_{1,2,3}$, and 14^-_1 states), or a $g_{7/2}$ neutron hole ($8^-_{1,3}$ and $14^-_{2,3}$ states).

The potential-energy surfaces for some of these states were plotted using the ULTIMATE CRANKER code [40,41] and are shown in Fig. 12. The trends in γ variation further indicate the γ-soft nature of this nucleus. For the even-mass Te isotopes with $A \leqslant 122$, the 16^+ state was interpreted to be of noncollective oblate shape with $\gamma = 60^\circ$ [13,42,43] based on the $\pi[(g_{7/2}d_{5/2})^2]_{6^+} \bigotimes \nu[(h^2_{11/2}]_{10^+}$ configuration. As seen in Fig. 11, the 16^+ state is not a favored terminating state in ^{126}Te. In CNSB calculations, the 16^+ state was suggested to be a collective one for ^{124,126}Te. Shell-model calculations suggest a most probable configuration $\pi(d_{5/2})^2 \bigotimes \nu(g_{7/2})^8(d_{5/2})^6(d_{3/2})^4(s_{1/2})^2(h_{11/2})^4$. The other predicted aligned state at 22^+ was not observed in our experiment. A possible explanation would be that for heavier Te isotopes, the generation of angular momentum by alignment of particles is hindered by neutron occupancy in time-reversed states of the $\nu h_{11/2}$ orbitals.

In Fig. 13, excitation energies relative to a rigid rotor have been plotted for the negative-parity band in ^{122,124,126}Te. Shallow minima have been observed at spin 9^- for ^{122}Te and ^{126}Te. Minima are also observed at spin values 11^- and 15^- for ^{126}Te [most probable configuration for both is $\pi(d_{5/2})^2 \bigotimes \nu(g_{7/2})^8(d_{5/2})^6(d_{3/2})^3(s_{1/2})^2(h_{11/2})^5$] which may

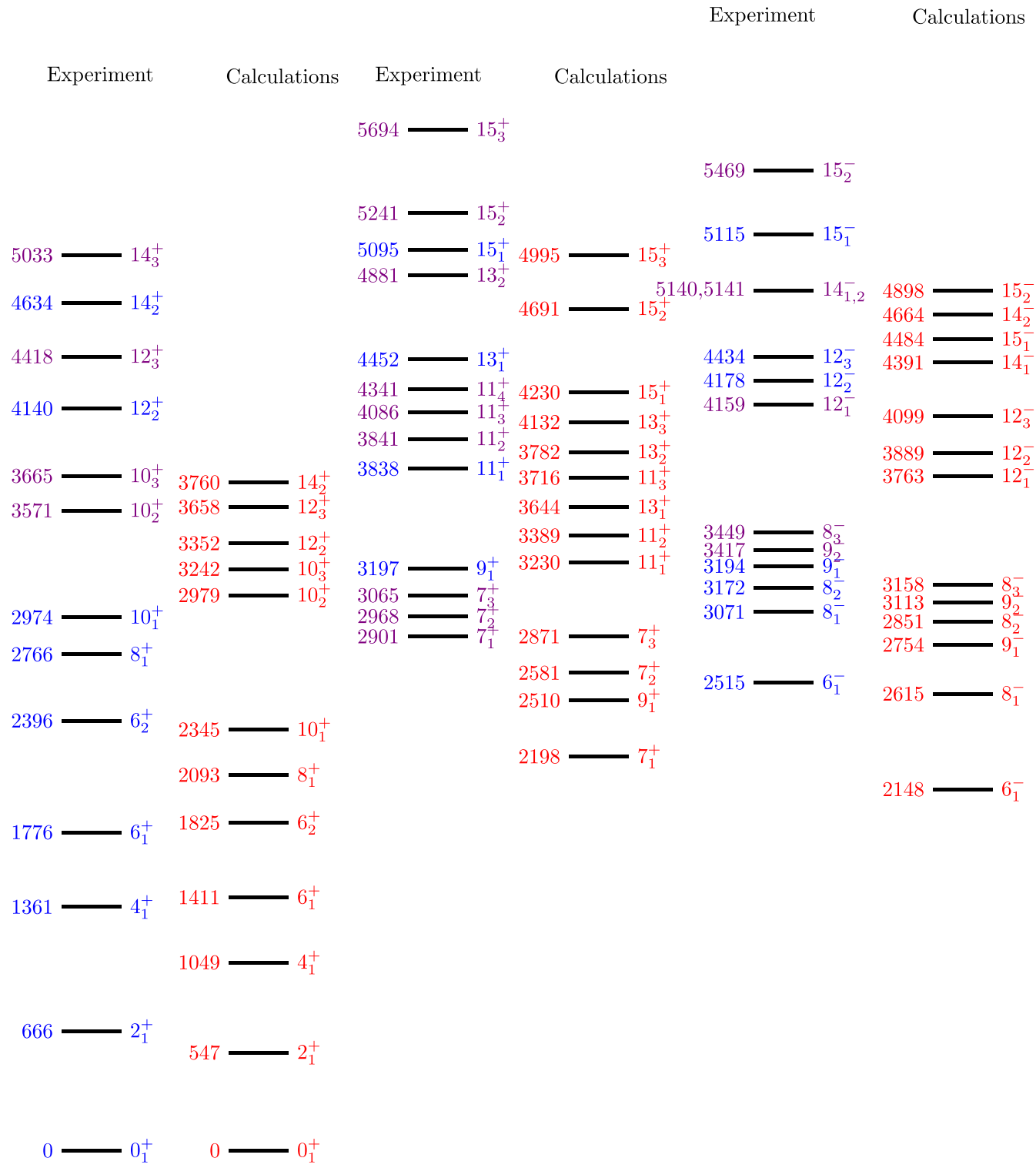

FIG. 10. Experimental energy levels and shell-model calculations for some of the levels of ^{126}Te. Newly observed experimental levels obtained in the present work are indicated in violet. The energy values have been rounded off to the nearest integer for brevity.

indicate possible aligned states, resulting from the breaking of a neutron pair [27]. A low-lying noncollective oblate state at 14^- has been predicted in Te isotopes with $A \leqslant 120$ [43]. However, these states have not been observed in heavier-mass Te isotopes.

A. Comments on the model calculations and scope for improvements

To study the effect of various truncations on the energy levels and wave functions, we obtained results from different sets of truncations. In a particular case, the proton subspace

TABLE II. Occupation of some of the experimentally observed states using shell-model code ANTOINE [34]. The wave function corresponding to the most probable configuration is used. Only states with an occupation probability $\geqslant 1\%$ are considered.

State	Probability (%)	Wave function
	Positive-parity states	
7_1^+	12.6	$\pi(g_{7/2})^1(d_{5/2})^1\ \nu(g_{7/2})^8\nu(d_{5/2})^6\nu(d_{3/2})^2\nu(s_{1/2})^2\nu(h_{11/2})^6$
7_2^+	8.1	$\pi(g_{7/2})^2\ \nu(g_{7/2})^8\nu(d_{5/2})^6\nu(d_{3/2})^2\nu(s_{1/2})^2\nu(h_{11/2})^6$
7_3^+	12.1	$\pi(g_{7/2})^1(d_{5/2})^1\ \nu(g_{7/2})^8\nu(d_{5/2})^6\nu(d_{3/2})^4\nu(s_{1/2})^2\nu(h_{11/2})^4$
9_1^+	12.7	$\pi(d_{5/2})^2\ \nu(g_{7/2})^8\nu(d_{5/2})^6\nu(d_{3/2})^4\nu(s_{1/2})^2\nu(h_{11/2})^4$
11_1^+	8.6	$\pi(d_{5/2})^2\ \nu(g_{7/2})^6\nu(d_{5/2})^6\nu(d_{3/2})^4\nu(s_{1/2})^2\nu(h_{11/2})^6$
11_2^+	14.5	$\pi(g_{7/2})^1(d_{5/2})^1\ \nu(g_{7/2})^8\nu(d_{5/2})^6\nu(d_{3/2})^2\nu(s_{1/2})^2\nu(h_{11/2})^6$
11_3^+	10.9	$\pi(g_{7/2})^1(d_{5/2})^1\ \nu(g_{7/2})^8\nu(d_{5/2})^6\nu(d_{3/2})^2\nu(s_{1/2})^2\nu(h_{11/2})^6$
13_1^+	23.2	$\pi(g_{7/2})^1(d_{5/2})^1\ \nu(g_{7/2})^8\nu(d_{5/2})^6\nu(d_{3/2})^4\nu(s_{1/2})^2\nu(h_{11/2})^4$
13_2^+	11.9	$\pi(g_{7/2})^1(d_{5/2})^1\ \nu(g_{7/2})^7\nu(d_{5/2})^6\nu(d_{3/2})^3\nu(s_{1/2})^2\nu(h_{11/2})^6$
13_3^+	22.7	$\pi(g_{7/2})^1(d_{5/2})^1\ \nu(g_{7/2})^8\nu(d_{5/2})^6\nu(d_{3/2})^4\nu(s_{1/2})^2\nu(h_{11/2})^4$
15_1^+	24.2	$\pi(g_{7/2})^1(d_{5/2})^1\ \nu(g_{7/2})^8\nu(d_{5/2})^6\nu(d_{3/2})^4\nu(s_{1/2})^2\nu(h_{11/2})^4$
15_2^+	24.2	$\pi(g_{7/2})^1(d_{5/2})^1\ \nu(g_{7/2})^8\nu(d_{5/2})^6\nu(d_{3/2})^4\nu(s_{1/2})^2\nu(h_{11/2})^4$
15_3^+	14.9	$\pi(g_{7/2})^1(d_{5/2})^1\ \nu(g_{7/2})^8\nu(d_{5/2})^6\nu(d_{3/2})^2\nu(s_{1/2})^2\nu(h_{11/2})^6$
	Negative-parity states	
6_1^-	25.4	$\pi(d_{5/2})^2\ \nu(g_{7/2})^8\nu(d_{5/2})^6\nu(d_{3/2})^3\nu(s_{1/2})^2\nu(h_{11/2})^5$
8_1^-	24.7	$\pi(d_{5/2})^2\ \nu(g_{7/2})^7\nu(d_{5/2})^6\nu(d_{3/2})^4\nu(s_{1/2})^2\nu(h_{11/2})^5$
8_2^-	17.2	$\pi(d_{5/2})^2\ \nu(g_{7/2})^8\nu(d_{5/2})^6\nu(d_{3/2})^3\nu(s_{1/2})^2\nu(h_{11/2})^5$
8_3^-	11.4	$\pi(d_{5/2})^2\ \nu(g_{7/2})^7\nu(d_{5/2})^6\nu(d_{3/2})^4\nu(s_{1/2})^2\nu(h_{11/2})^5$
12_1^-	22.7	$\pi(g_{7/2})^1(d_{5/2})^1\ \nu(g_{7/2})^8\nu(d_{5/2})^6\nu(d_{3/2})^3\nu(s_{1/2})^2\nu(h_{11/2})^5$
12_2^-	17.3	$\pi(g_{7/2})^1(d_{5/2})^1\ \nu(g_{7/2})^8\nu(d_{5/2})^6\nu(d_{3/2})^3\nu(s_{1/2})^2\nu(h_{11/2})^5$
12_3^-	22.4	$\pi(d_{5/2})^2\ \nu(g_{7/2})^8\nu(d_{5/2})^6\nu(d_{3/2})^3\nu(s_{1/2})^2\nu(h_{11/2})^5$
14_1^-	24.5	$\pi(d_{5/2})^2\ \nu(g_{7/2})^8\nu(d_{5/2})^6\nu(d_{3/2})^3\nu(s_{1/2})^2\nu(h_{11/2})^5$
14_2^-	24.5	$\pi(d_{5/2})^2\ \nu(g_{7/2})^7\nu(d_{5/2})^6\nu(d_{3/2})^4\nu(s_{1/2})^2\nu(h_{11/2})^5$
14_3^-	14.4	$\pi(d_{5/2})^2\ \nu(g_{7/2})^7\nu(d_{5/2})^6\nu(d_{3/2})^4\nu(s_{1/2})^2\nu(h_{11/2})^5$

consisted of three orbitals $g_{7/2}$, $d_{5/2}$, and $h_{11/2}$ while the neutron subspace consisted of all five orbitals: $g_{7/2}$, $d_{5/2}$, $d_{3/2}$, $s_{1/2}$, and $h_{11/2}$. The parameters were chosen to allow states with the $\nu h_{11/2}$ orbitals to be completely filled while states with eight neutrons or less in $h_{11/2}$ were severely truncated. The results for the new truncations are shown in Fig. 14. We note the following observations:

(i) The shell-model truncations used in the present work (Fig. 10 and Table II) suggest a configuration involving the coupling of two $g_{7/2}$ holes for the 2_1^+ and 4_1^+ states. However, with the new truncations a notable result observed is the better agreement of the 2_1^+ and 4_1^+ state energies with their experimental counterparts. The most probable configurations for both the 2_1^+ and 4_1^+ states are $\pi(g_{7/2})^2 \bigotimes \nu(g_{7/2})^8(d_{5/2})^4(h_{11/2})^{12}$. The probabilities for the states are 35% and 44%, respectively. The model predicts the $B(E2; 2_1^+ \rightarrow 0_1^+)$ and $B(E2; 4_1^+ \rightarrow 2_1^+)$ values as 25.3 and 24.8 W.u., respectively for the new set of truncations. The effective charges were changed from the original calculations to $1.9e$ for protons and $1.27e$ for neutrons to get better results.

(ii) The experimental and theoretical agreement between the higher positive-parity spins from 6^+ onwards and the negative-parity states, however, are considerably worse. The energy differences between theory and experiment come out to be $\approx$5000 keV for the negative-parity states.

The interactions between the valence nucleons result in collective effects that eventually affect the nuclear shape, with the intruder $h_{11/2}$ orbitals having a greater effect on the overall shape of the nucleus. With the $h_{11/2}$ orbitals completely filled, the shell is rendered inert with respect to its polarization effects on the nuclear core. This would suggest a coupling of the two neutron holes in $d_{5/2}$ to form the 2^+ and 4^+ states. For the higher spin states from 6^+ onwards, the matrix elements between the $h_{11/2}$ and other orbitals become largely attractive, which greatly underestimates the binding energies of the states. This is observed in the variation of the experimental excitation energies with respect to the corresponding calculated ones (Fig. 15), which shows an approximately linear trend with energy differences increasing with spin. The very large discrepancy for the negative-parity states using the new truncations is due to the complete exclusion of states having

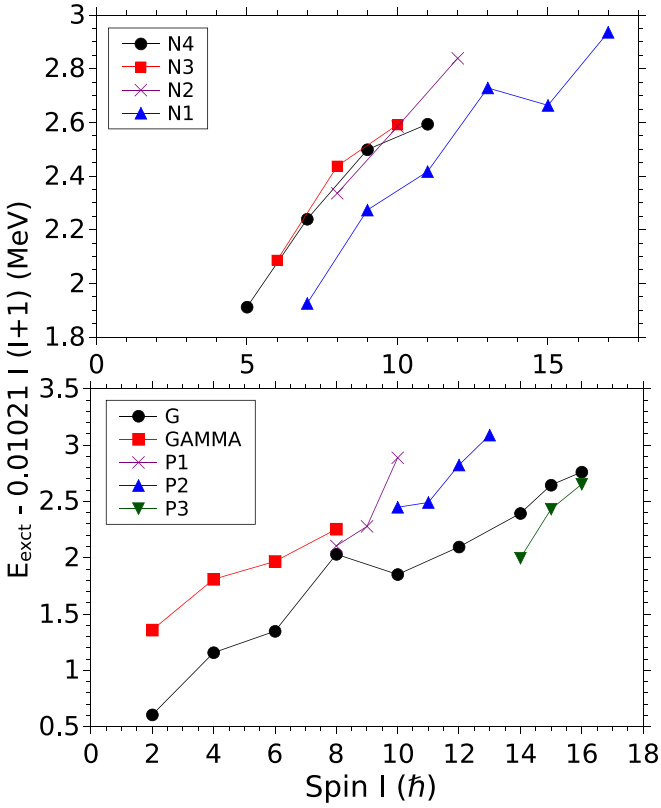

FIG. 11. Experimental excitation energy relative to a rigid-rotor plotted against spin for the negative (top panel) and positive (bottom panel) structures. The total energy of a rigid rotor was calculated as $\approx 32.32A^{-5/3}$I (I + 1) [36].

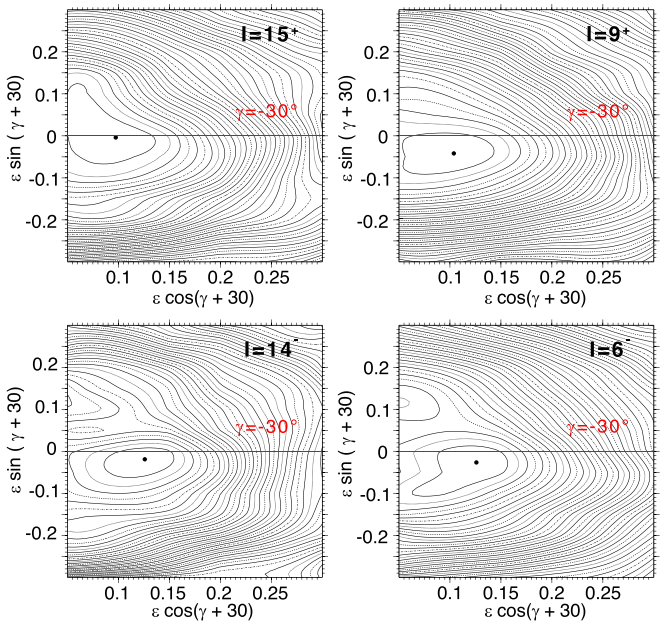

FIG. 12. The potential-energy surfaces for some of the positive and negative-parity parity states obtained using the ultimate Cranker code. The γ values for the negative-parity states (bottom panel) vary from $-41.4°$ for 6^- to $-39.7°$ for 14^- while for the positive-parity states (top panel), the values range from $-52.1°$ for 9^+ to $-32.7°$ for 15^+.

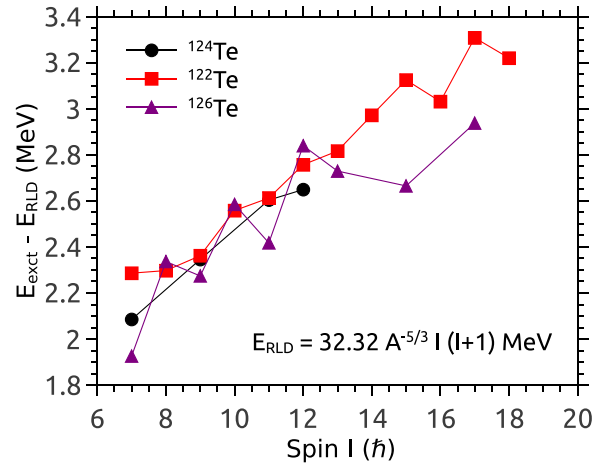

FIG. 13. Experimental excitation energy relative to a rigid rotor plotted against spin for negative-parity bands (based on the 7^- level in ^{122,124,126}Te.

odd number of neutrons in $h_{11/2}$. These discrepancies in a truncated model space may be countered by using fine-tuned matrix elements and inclusion of three-body forces [38,39], as stated earlier, which can produce better results for some of the levels.

The model does not take into account the effects of 2p-2h or 1p-1h core excitations which are observed in the $Z = 50$ region [44]. Such excitations have been observed in ^{122}Te, where a sequence of dipole transitions was suggested to be based on a proton 3p-1h configuration [43]. The structures P1-P3 are similarly suggested to be based on configurations with one hole in $g_{9/2}$.

B. Transition probabilities

The reduced transition probabilities $B(E2)$ were calculated using the shell-model code ANTOINE [34]. A previous work found that the experimental $B(E2)$ values were more sensitive to the neutron effective charge value. The obtained results generally agreed better with the calculated ones, when using effective charges $1.5e$ for protons and $1.0e$ for neutrons [35]. We have used the same values for our calculations. The results are given in Table III. The experimental $B(E2; 2_1^+ \rightarrow$

TABLE III. Comparison of $B(E2)$ values obtained from experiment and shell model calculations.

Transition	Experiment (W.u.)	Calculations (W.u.)
$B(E2; 2_1^+ \rightarrow 0_1^+)$	25.4^{+7}_{-7} [a]	22.6
$B(E2; 2_2^+ \rightarrow 2_1^+)$	45^{+5}_{-4} [a]	30.3
$B(E2; 4_1^+ \rightarrow 2_1^+)$	34^{+28}_{-28} [a]	29.6
$B(E2; 4_2^+ \rightarrow 4_1^+)$	12.0^{+10}_{-9} [a]	12.8
$B(E2; 4_2^+ \rightarrow 2_1^+)$	3.7^{+3}_{-3} [a]	3.3
$B(E2; 10_1^+ \rightarrow 8_1^+)$	3.57(5) [b]	10.12
$B(E2; 10_1^+ \rightarrow 8_2^+)$	0.46(1) [b]	6.56

[a]Obtained from Ref. [45].
[b]$B(E2)$ calculated using half-life value obtained from the National Nuclear Data Centre (NNDC) site.

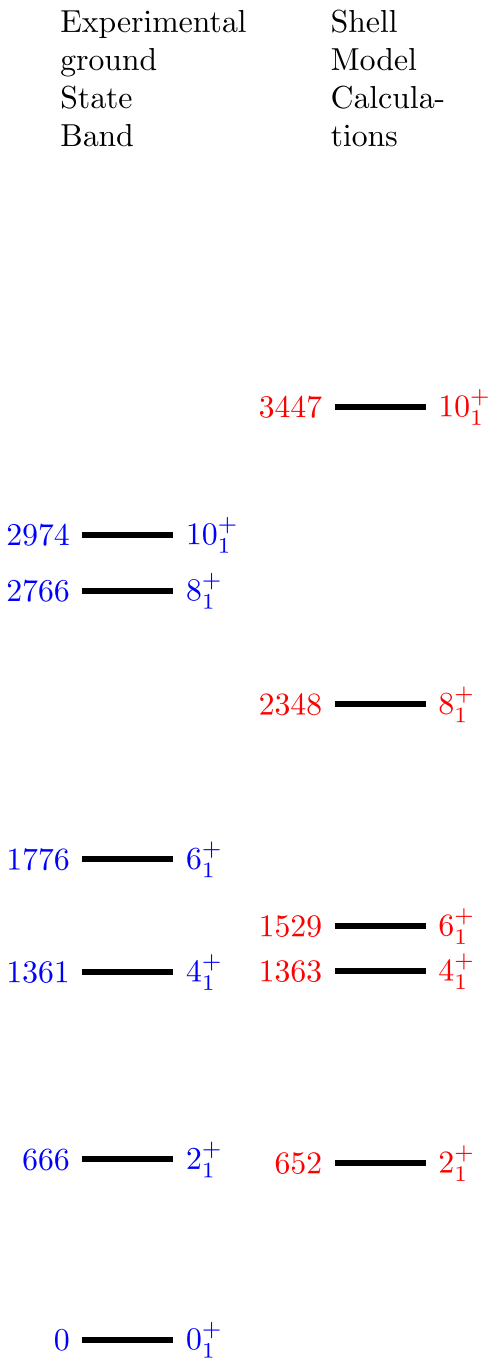

FIG. 14. A comparison of the experimental level energies with the shell-model results for the new truncations.

0_1^+) and $B(E2; 4_1^+ \rightarrow 2_1^+)$ values show fairly good agreement with calculations. The ratio $B(E2; 4_1^+ \rightarrow 2_1^+)/B(E2; 2_1^+ \rightarrow 0_1^+)$ comes out to be 1.34 experimentally, while it is 1.31 in the calculations. This value is close to ≈1.5, as expected for a nucleus exhibiting E(5) critical-point symmetry [20]. In the experiment, two transitions to the 8_1^+ and 8_2^+ states have been observed from the isomeric 10_1^+ state [half-life = 10.7(9) ns]. The 134.1-keV transition was not previously observed and is a new transition verified in our work. The branching ratios for the 134.1- and 208.6-keV transitions were calculated and used

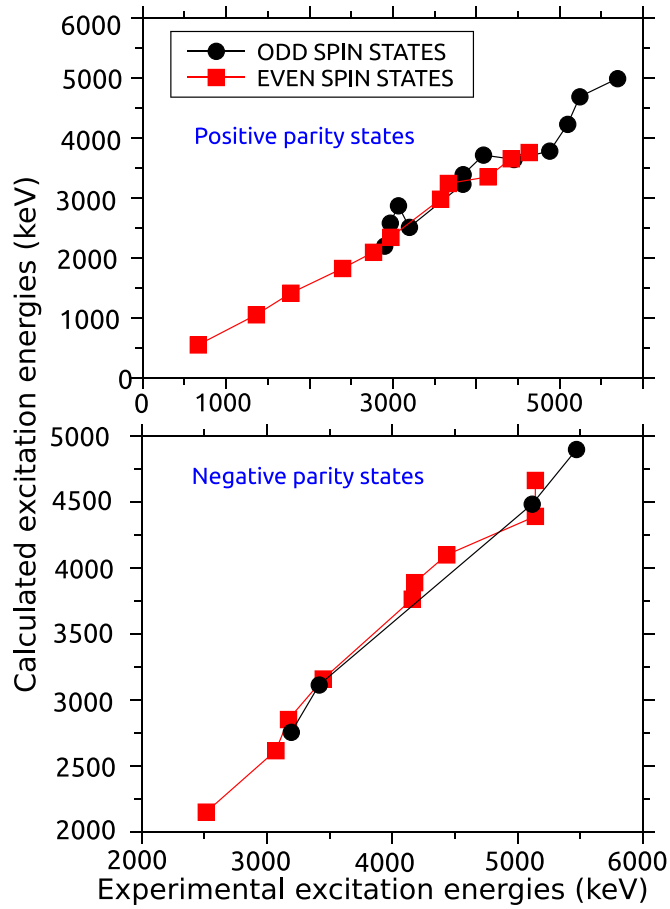

FIG. 15. A comparison of the experimental and shell-model excitation energies obtained in the present work.

to determine the experimental $B(E2)$ ratios. The calculated values for both $B(E2; 10_1^+ \rightarrow 8_1^+)$ and $B(E2; 10_1^+ \rightarrow 8_2^+)$ are greater than the experimental values for the same. The high values of the $B(E2)$ transition rates for the 8^+ and 10^+ indicate an involvement of the proton components of the wave function [27].

VI. SUMMARY

The excited states of ^{126}Te were populated in an alpha-induced fusion-evaporation reaction ^{124}Sn$(\alpha, 3n/2n)$ ^{125,126}Te at a beam energy of 31 MeV. The deexciting gammas were detected by the INGA array. The previously known level scheme was subsequently enriched with the placement of 65 new transitions. Spin and parity assignments were done using DCO and IPDCO ratios. Detection of some new transitions and reevaluation of some of the properties of the previously established ones have led to changes in spin-parity assignments of the levels. Five possible new structures have also been suggested. Shell-model calculations were carried out using the code ANTOINE. The components of the wave functions corresponding to the various spin values have been identified. $B(E2)$ values from calculations show a fair agreement with those obtained in the literature. Further experimental studies to enrich the higher spin states of the new structures may be carried out to gain insight into their nature.

ACKNOWLEDGMENTS

A.D. acknowledges the MHRD, Government of India, for financial support. S. Nag acknowledges the financial support from the SERB-DST, India under CRG (File No. CRG/2021/006671). The authors would like to express their gratitude to the INGA Collaboration for the arrangement of the experiment and setting up the INGA at VECC, India. The authors acknowledge the support of the staff at VECC during the experiment.

[1] M. Houry, R. Lucas, M.-G. Porquet, C. Theisen, M. Girod, M. Aiche, M. Aleonard, A. Astier, G. Barreau, F. Becker, J. Chemin, I. Deloncle, T. Doan, J. Durell, K. Hauschild, W. Korten, Y. Coz, M. Leddy, S. Perries, and B. Varley, Eur. Phys. J. A **6**, 43 (1999).

[2] T. Naz, G. Bhat, S. Jehangir, S. Ahmad, and J. Sheikh, Nucl. Phys. A **979**, 1 (2018).

[3] P. E. Garrett *et al.*, Phys. Rev. Lett. **123**, 142502 (2019).

[4] P. Kumar and S. K. Dhiman, Nucl. Phys. A **1001**, 121935 (2020).

[5] T. Loennroth *et al.*, *Finnish Physical Society Conference Proceedings* (Oulu University, Finland, 1991).

[6] L. P. Gaffney *et al.*, Phys. Rev. C **89**, 024307 (2014).

[7] N. Ashok, S. P, and A. Joseph, DAE Symp. Nucl. Phys. **64**, 62 (2019).

[8] J. E. García-Ramos and K. Heyde, Phys. Rev. C **92**, 034309 (2015).

[9] J. Wood, K. Heyde, W. Nazarewicz, M. Huyse, and P. van Duppen, Phys. Rep. **215**, 101 (1992).

[10] K. Heyde and J. L. Wood, Rev. Mod. Phys. **83**, 1467 (2011).

[11] A. de Shalit and M. Goldhaber, Phys. Rev. **92**, 1211 (1953).

[12] R. Bengtsson, Intruder states and low energy nuclear spectroscopy, in *Nuclear Shapes and Nuclear Structure at Low Excitation Energies* (Springer US, Boston, 1992), pp. 123–141.

[13] S. Nag, P. Singh, K. Selvakumar, A. K. Singh, A. Bisoi, A. Goswami, S. Bhattacharya, S. Kumar, K. Singh, J. Sethi, S. Saha, T. Trivedi, S. V. Jadhav, R. Donthi, B. S. Naidu, and R. Palit, Eur. Phys. J. A **49**, 145 (2013).

[14] H. Sabri, Z. Jahangiri, and M. Mohammadi, Nucl. Phys. A **946**, 11 (2015).

[15] M. Saxena, R. Kumar, A. Jhingan, S. Mandal, A. Stolarz, A. Banerjee, R. K. Bhowmik, S. Dutt, J. Kaur, V. Kumar, M. Modou Mbaye, V. R. Sharma, and H.-J. Wollersheim, Phys. Rev. C **90**, 024316 (2014).

[16] J. Honzátko, V. Bondarenko, I. Tomandl, T. von Egidy, H.-F. Wirth, D. Bucurescu, V. Ponomarev, N. Mărginean, R. Hertenberger, Y. Eisermann, G. Graw, and L. Rubacek, Nucl. Phys. A **756**, 249 (2005).

[17] F. Iachello, Phys. Rev. Lett. **85**, 3580 (2000).

[18] F. Iachello, Phys. Rev. Lett. **87**, 052502 (2001).

[19] R. F. Casten and N. V. Zamfir, Phys. Rev. Lett. **85**, 3584 (2000).

[20] R. M. Clark, M. Cromaz, M. A. Deleplanque, M. Descovich, R. M. Diamond, P. Fallon, I. Y. Lee, A. O. Macchiavelli, H. Mahmud, E. Rodriguez-Vieitez, F. S. Stephens, and D. Ward, Phys. Rev. C **69**, 064322 (2004).

[21] S. Das, S. Samanta, R. Banik, R. Bhattacharjee, K. Basu, R. Raut, S. Ghugre, A. Sinha, S. Bhattacharya, S. Imran, G. Mukherjee, S. Bhattacharyya, A. Goswami, R. Palit, and H. Tan, Nucl. Instrum. Methods Phys. Res., Sect. A **893**, 138 (2018).

[22] A. Krämer-Flecken, T. Morek, R. Lieder, W. Gast, G. Hebbinghaus, H. Jäger, and W. Urban, Nucl. Instrum. Methods Phys. Res., Sect. A **275**, 333 (1989).

[23] P. Ray *et al.*, Phys. Rev. C **101**, 064313 (2020).

[24] R. Banik *et al.*, Phys. Rev. C **101**, 044306 (2020).

[25] D. Radford, Nucl. Instrum. Methods Phys. Res., Sect. A **361**, 297 (1995).

[26] A. Kerek, Nucl. Phys. A **176**, 466 (1971).

[27] A. Astier, M. Porquet, T. Venkova, C. Theisen, G. Duchêne, F. Azaiez, G. Barreau, D. Curien, I. Deloncle, O. Dorvaux, B. Gall, M. Houry, R. Lucas, N. Redon, M. Rousseau, and O. Stezowski, Eur. Phys. J. A **50**, 2 (2013).

[28] L.-C. He, Y. Zheng, L.-H. Zhu, H.-L. Ma, X.-G. Wu, C.-Y. He, G.-S. Li, L.-L. Wang, X. Hao, Y. Liu, X.-Q. Li, B. Pan, Z.-Y. Li, and H.-B. Ding, Chin. Phys. C **41**, 044003 (2017).

[29] H. Iimura, J. Katakura, and S. Ohya, Nucl. Data Sheets **180**, 1 (2022).

[30] S. S. Tiwary, H. P. Sharma, S. Chakraborty, C. Majumder, G. H. Bhat, J. A. Sheikh, P. Baneerjee, S. Ganguly, S. Rai, Pragati, Mayank, S. Kumar, A. Kumar, S. S. Bhattacharjee, R. P. Singh, and S. Muralithar, Eur. Phys. J. A **55**, 163 (2019).

[31] S. Nag *et al.*, Phys. Rev. C **85**, 014310 (2012).

[32] S. Nag *et al.*, Phys. Rev. C **88**, 044335 (2013).

[33] H. Kusakari, N. Yoshikawa, H. Kawakami, M. Ishihara, Y. Shida, and M. Sakai, Nucl. Phys. A **242**, 13 (1975).

[34] E. Caurier, M. Rejmund, and H. Grawe, Phys. Rev. C **67**, 054310 (2003).

[35] V. Kumar, P. Srivastava, M. Ermamatov, and I. Morales, Nucl. Phys. A **942**, 1 (2014).

[36] I. Ragnarsson, Z. Xing, T. Bengtsson, and M. A. Riley, Phys. Scr. **34**, 651 (1986).

[37] C. Qi, Phys. Rev. C **94**, 034310 (2016).

[38] A. Polls, H. Müther, A. Faessler, T. Kuo, and E. Osnes, Nucl. Phys. A **401**, 124 (1983).

[39] V. G. Zelevinsky, Phys. At. Nucl. **72**, 1107 (2009).

[40] T. Bengtsson, Nucl. Phys. A **496**, 56 (1989).

[41] T. Bengtsson, Nucl. Phys. A **512**, 124 (1990).

[42] N. Fotiades, J. A. Cizewski, R. Krücken, R. M. Clark, P. Fallon, I. Y. Lee, A. O. Macchiavelli, and W. Younes, Phys. Rev. C **89**, 017303 (2014).

[43] E. S. Paul, D. B. Fossan, G. J. Lane, J. M. Sears, I. Thorslund, and P. Vaska, Phys. Rev. C **53**, 1562 (1996).

[44] K. Heyde, C. De Coster, J. L. Wood, and J. Jolie, Phys. Rev. C **46**, 2113 (1992).

[45] J. R. Vanhoy, J. A. Tanyi, K. A. Crandell, T. H. Churchill, S. F. Hicks, M. C. Burns, P. A. Roddy, N. V. Warr, T. B. Brown, and S. R. Lesher, Phys. Rev. C **69**, 064323 (2004).